Final Technical Report
Oct 30, 2006
Period: Oct. 1, 2005-Oct. 1, 2006

Joining of Ion Transport Membranes Using a Novel Transient Liquid Phase Process

Principal Investigator: Darryl P. Butt,

Organization: Boise State University, 1910 University Drive, Boise, ID

83725-2075

Graduate Student: Patrick Callahan

Innovative Concepts Phase I Program: Joining and Sealing High

Temperature Gas Separation Membranes (DE-FG26-05NT42536)

Table of Contents

Abstract

The feasibility of a novel transient liquid phase (TLP) joining method has been demonstrated in joining $La_{0.9}Ca_{0.1}FeO_3$ materials. Metal oxide powders were processed to form the TLP compositions which were used in the joining process. The method has been successful in producing joint interfaces that effectively disappear, as they are the same material and have the same properties as the joined parts. The feasibility of the method has been demonstrated for a single system, but many systems where the method can potentially be applied have been identified.

1. Executive Summary

1.1 Project Objectives

The objective of this research is to demonstrate the feasibility of using a novel transient liquid phase method for joining ion transport membranes. There are several tasks to demonstrate the feasibility.

Task 1. (Title: Survey of Thermodynamics Systems) Survey of thermodynamics literature and phase diagrams of membrane materials systems to assess where TLP technology could potentially be applied.

Task 2. (Title: Synthesis of TLP compositions) Synthesize TLP compositions using mixed metal oxide processing methods.

Task 3. (Title: Quantification of TLP Wetting) Characterize the wetting of TLP compositions on substrate materials.

Task 4. (Title: Fabrication of Joined ITM Materials) Fabricate hermetic joints via the TLP process.

Task 5. (Title: Interfacial Characterization) Characterize the joint microstructure by scanning electron microscopy.

1.2 Introduction

Joining is an enabling technology for many ceramics applications. Often ceramics are only useful in a system of components, requiring that they be bonded in some fashion to other ceramic components of the same composition or dissimilar materials such as metals or other ceramics. This is particularly true in the practical applications of fuel cells, gas separation membranes, and sensors, where a wide variety of ceramic-ceramic and ceramic-metal joints are required.

There are a variety of existing methods for joining ceramics to themselves or other materials. For example, brazes and glasses are commonly used. These joining methods have the disadvantage of leaving behind an interfacial phase with thermal and physical

properties often inferior to those of the materials being joined. For example, brazes may oxidize or leave behind a ductile metal, which can creep or become incompatible with the surrounding materials at high temperatures. Similarly, glass seals may have significantly different thermal expansion coefficients compared with surrounding materials resulting in undesirable residual stresses, will soften and creep at temperatures above their respective glass transition temperature, and can be chemically incompatible at elevated temperatures.

Consequently, industry and academia have sought for many years to develop joining methods which leave behind effectively no interfacial phase or a compatible, refractory phase with virtually the same thermal expansion coefficient as and other attributes of the joined parts. This proposed method accomplishes that goal through a novel, transient liquid phase (TLP) approach.

The objective of this proposed research is to develop a reliable transient liquid phase (TLP) or partially transient liquid phase (PTLP) process to join ceramic materials to themselves or to materials of similar or compatible compositions leaving behind no interfacial phase or a compatible, refractory interfacial phase. The materials of primary interest to this study are ion conducting materials, particularly perovskites for use in high temperature applications. However, the joining technology may be useful for a wide variety of other ceramic membranes systems as well as other ceramic systems in general.

In addition to joining, the technology could be used to repair, weld or mend ceramic components. Also the TLP concept could be used to reduce the sintering temperature of ion transport membranes. These additional potential benefits are not addressed in this work, but it is a logical extension of the research.

1.3 Background

TLP joining is often superior to other joining methods because it can produce a joint interface with the same or similar properties as the joined materials. This is possible in other joining processes such as diffusion bonding or the use of nanocrystalline interlayers only through the use of high temperatures and applied pressures or clamping forces during joining. TLP joining avoids the need for clamping forces or expensive equipment like hot presses because at the joining temperature a liquid phase forms at the interface and fills gaps and voids.

Parts to be joined have a TLP material applied at their interface. The assembly is heated to the joining temperature, at which point a liquid phase is formed at the interface. The liquid phase fills gaps at the interface and diffuses into surrounding materials. As the liquid phase diffuses into the surrounding materials, the interface solidifies isothermally into a material of similar or compatible composition to that of the joined materials, leaving behind no interfacial phase or a compatible, refractory interfacial phase. TLP joints can have use temperatures that approach or can exceed the joining temperature as the joint solidifies isothermally at the joining temperature.

Traditionally diffusion of both the interface material and the surrounding materials into each other leads to an interface with properties similar to those of the joined parts. The method discussed here achieves this by joining a material to the same material with a TLP material that isothermally solidifies to form the same material as those joined. The Lanthanum Calcium Ferrite (LCF) perovskite system ($La_xCa_{1-x}FeO_3$) was joined to itself to demonstrate the feasibility of the TLP method discussed here. LCFs are used as separation membranes for Syngas production, so the assemblies need to operate at high temperatures. Therefore, the joint interface needs to resist creep, avoid problems with thermal cycling, and be chemically stable in the high temperature environment. Ideally, the interface in such systems is the same as the parts in the assembly.

1.4 Accomplishments

A survey of thermodynamics literature was conducted to determine potential TLP systems other than the Fe_2O_3-CaO-La_2O_3 system. The information gathered was assembled into a matrix that includes melting points at various compositions.

La, Ca, and Fe oxide powders were processed into TLP compositions. The process involved mixing, calcining and with the addition of a ball mill to our lab, milling the powders as well. These milled TLP compositions were used to produce inks, joints, pellets, and study wetting behavior.

The processed TLP powders were used in pellet production. Pellets of the $La_{0.9}Ca_{0.1}FeO_3$ perovskite were produced by pressing then sintering the TLP compositions at various times and temperatures. XRD was performed on the sintered pellets and used to find an activation energy for perovskite formation. The activation energy was found to be 108 kJ/mol.

Wetting of $La_{0.9}Ca_{0.1}FeO_3$ substrates was studied. The TLP compositions were found to thoroughly wet the substrates, indicating that the liquid phase fills the joint interfacial region leading to joint uniformity and little interfacial porosity and few interfacial gaps.

Monolithic specimens of $La_{0.9}Ca_{0.1}FeO_3$ provided by Ceramatec, Inc (see Figure 1)were joined using the processed powders. Many successful joints were produced. The joints were ideal, and in places the only thing that distinguished them from the joined parts was slight porosity. The dissimilar materials $La_{0.9}Ca_{0.1}FeO_3$ and alumina were joined using the TLP method as well.

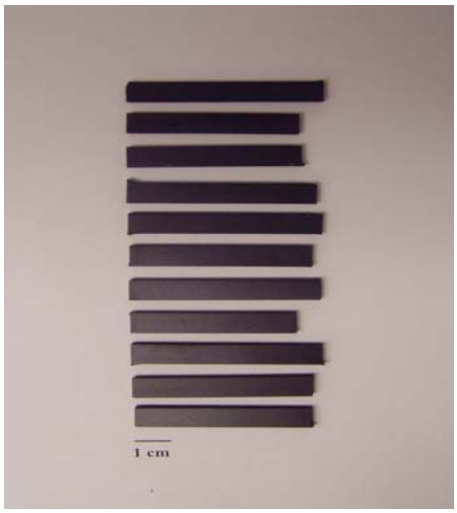

Figure 1. $La_{0.9}Ca_{0.1}FeO_3$ pieces fabricated at Ceramatec, Inc.

2. Report Details

2.1 Experimental methods

2.1.1 Potential TLP Systems

A list of materials used in the development of transport membranes was compiled. These materials were used as a basis to search phase diagram literature for candidate systems of materials where the TLP process could be applied. Possible systems usually have a eutectic point at which the liquid phase dissolves into the surrounding materials and forms a more refractory material. The data were compiled into a document for reference (See Appendix A). The candidate system $CaO\text{-}Fe_2O_3\text{-}La_2O_3$ was used to demonstrate the feasibility of the TLP method discussed here.

2.1.2 Synthesis of TLP Compositions and Inks

Processing powders into their TLP compositions takes place in several steps. First, the unprocessed powders are mixed into two compositions. The unprocessed powders are $CaCO_3$, Fe_2O_3, and La_2O_3. The two different powder compositions are the flux phase, which produces a liquid phase at the joining temperature and the refractory phase, which does not form a liquid phase at the joining temperature. The flux phase is a combination of $CaO\text{-}Fe_2O_3$ and the refractory phase is a combination of La_2O_3- Fe_2O_3. Figure 2 shows a binary phase diagram for the $CaO\text{-}Fe_2O_3$ system.

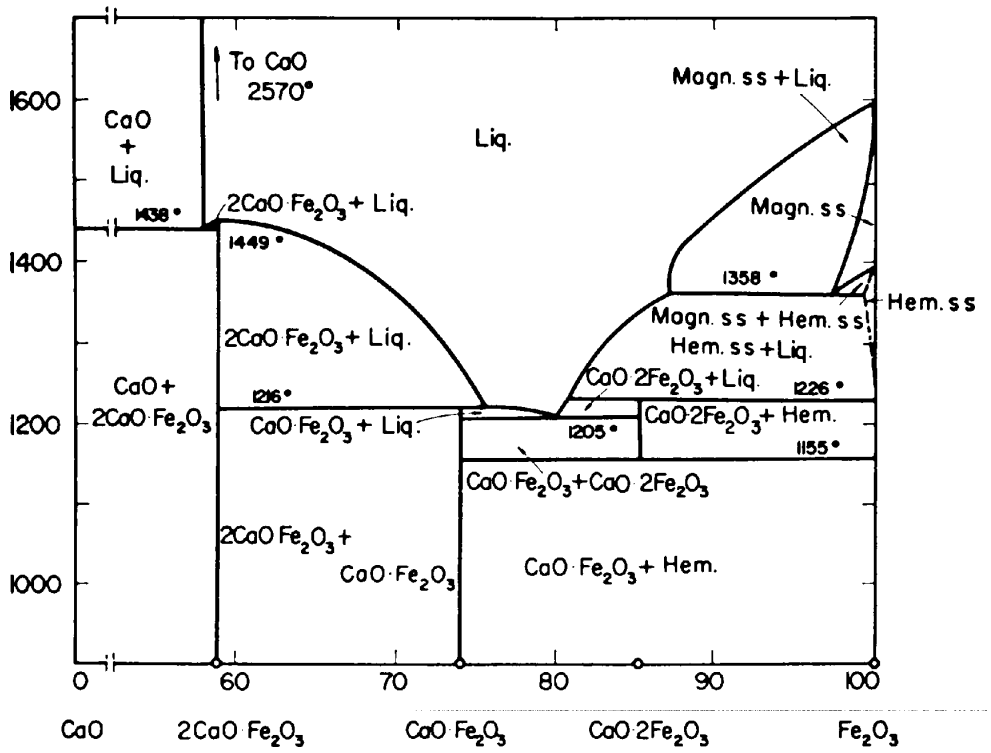

Figure 2: $CaO\text{-}Fe_2O_3$ binary phase diagram from B. Phillips and A. Muan.[6]

As observed in the $CaO\text{-}Fe_2O_3$ binary phase diagram, a liquid phase will form above 1205-1226°C in the $CaO\text{-}Fe_2O_3$ system at above approximately 59 weight percent (wt%) Fe_2O_3. Therefore, the flux phase is mixed so that it is above 59 wt% Fe_2O_3 and it will form a liquid phase above these temperatures. The amount of liquid phase present at the joining temperature can be controlled easily by changing the ratio of CaO and Fe_2O_3.

The materials being joined are $La_{0.9}Ca_{0.1}FeO_3$, so the preferred interface would also be $La_{0.9}Ca_{0.1}FeO_3$. Therefore, the flux and refractory phase amounts are chosen so that when combined they yield a stoichiometry of $La_{0.9}Ca_{0.1}FeO_3$. For example, a combination that yields the correct stoichiometry is when the flux consists of 78 wt% Fe_2O_3 and 22 wt% CaO and the refractory phase consists of 29 wt% Fe_2O_3 and 71 wt% La_2O_3.

The flux and refractory phases are milled separately by planetary ball milling in isopropanol to finer sizes. After milling they are calcined in air at 850°C to drive the dissociation reaction $CaCO_{3(s)} \rightarrow CaO_{(s)} + CO_{2(g)}$ and to evaporate any H_2O. After this the phases are mixed together in a mill and can be used to synthesize inks or tapes, and can be pressed into pellets for sintering studies.

The TLP compositions are combined with a solvent and binder. The formula used is 20% TLP by volume, 77% solvent, and 3% binder by volume. The solvent is 4 parts toluene and 1 part ethanol by weight, and the binder is a Butvar B-76 polyvinyl-butyral. These are thoroughly mixed together by paint shaking for an hour prior to use.

2.1.3 Sintering Studies

The processed TLP powders were used to make perovskite pellets. Approximately 1 gram of powder was pressed for 1 minute into 13mm diameter pellets with an applied pressure of approximately 335MPa. The pellets were then sintered in air at various times and temperatures. They were analyzed with Scanning Electron Microscopsy (SEM) to analyze the sintering progression of perovskite formation. X-Ray Diffraction analysis (XRD) was performed on the pellets. The peak intensities were used to find an activation energy of perovskite formation.

2.1.4 Wetting Behavior

To study wetting behavior a piece of the TLP composition or the flux phase is broken from a pellet which has been pressed in the same manner as for sintering studies. This piece is placed on a $La_{0.9}Ca_{0.1}FeO_3$ substrate and the substrate is heated above the melting point of the flux phase and a drop forms on the surface of the substrate. It is cooled to room temperature and the drop solidifies. The angle θ between the drop and the substrate, called the wetting angle, is measured (see Figure 3). If $\theta<90°$ the material is said to wet the surface of the substrate, and if $\theta>90°$ the material is said to be nonwetting. If $\theta=0°$, the ink is spreading, and the ink thoroughly wets the surface.

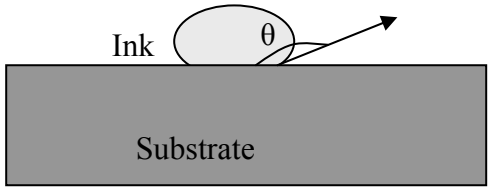

Figure 3: Schematic showing the wetting angle.

2.1.5 Joining

Pieces of monolithic $La_{0.9}Ca_{0.1}FeO_3$ were cut into approximately 7.7mm x 7.7mm x 2.8mm pieces. The surfaces of the pieces that would be joined were polished with progressively finer SiC grit paper to a final grit of 1200, then ultrasonically cleaned in acetone and rinsed with DI water. Then the ink is painted on the opposing surfaces of both pieces, xylene is painted on the surface, and the pieces are pressed together lightly as the xylene dries. The xylene interacts with the binder in the ink and causes a weak joint to form so the assembly can be handled until heating. The assembly is heated above the flux phase's melting point causing a liquid phase to form. A schematic of the process is shown in Figure 4.

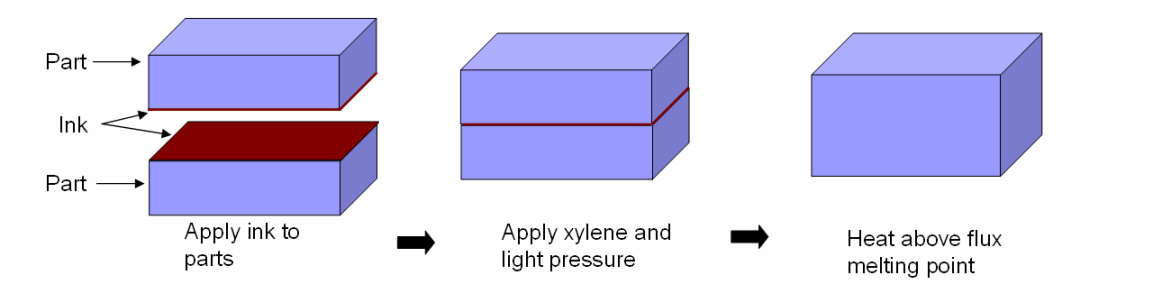

Figure 4: Schematic of joining two parts using an ink.

The liquid phase interacts with the refractory phase, the part surfaces, and fills gaps at the interface. It also allows the solid refractory phase to reposition itself into a more densely packed arrangement. The liquid phase diffuses into surrounding refractory phase and parts. The interface solidifies isothermally to $La_{0.9}Ca_{0.1}FeO_3$ as the liquid phase diffuses into the surrounding materials.

The integrity of the joint was tested manually. The joined assemblies were cut with a low speed diamond saw and polished for SEM characterization.

3. Results and Discussions

3.1 Potential TLP Systems

The survey of thermodynamics literature that was conducted discovered many potential systems where the TLP method can be applied. The results of this survey are attached as Appendix A. It included the Fe_2O_3-CaO-La_2O_3 system with which the method was demonstrated. It included many other materials systems, many of which are used in applications such as fuel cells and transport membranes.

3.2 Synthesis of TLP Compositions

Several batches of TLP compositions were made. Most were $La_{0.9}Ca_{0.1}FeO_3$ where the flux consisted of 78 wt% Fe_2O_3 and 22 wt% CaO and the refractory phase consisted of 29 wt% Fe_2O_3 and 71 wt% La_2O_3. There were others, including a batch where the flux phase was 94 wt% Fe_2O_3 and 6 wt% CaO. Also batches with nominal compositions of $La_{0.75}Ca_{0.25}FeO_3$ and $La_{0.9}Ca_{0.35}FeO_3$ were synthesized. It was verified by XRD that calcining the flux phase at 850°C caused the removal of CO_2 from the $CaCO_3$. XRD patterns of the flux phase before and after calcining are shown in Figures 5 and 6 with the peaks identified.

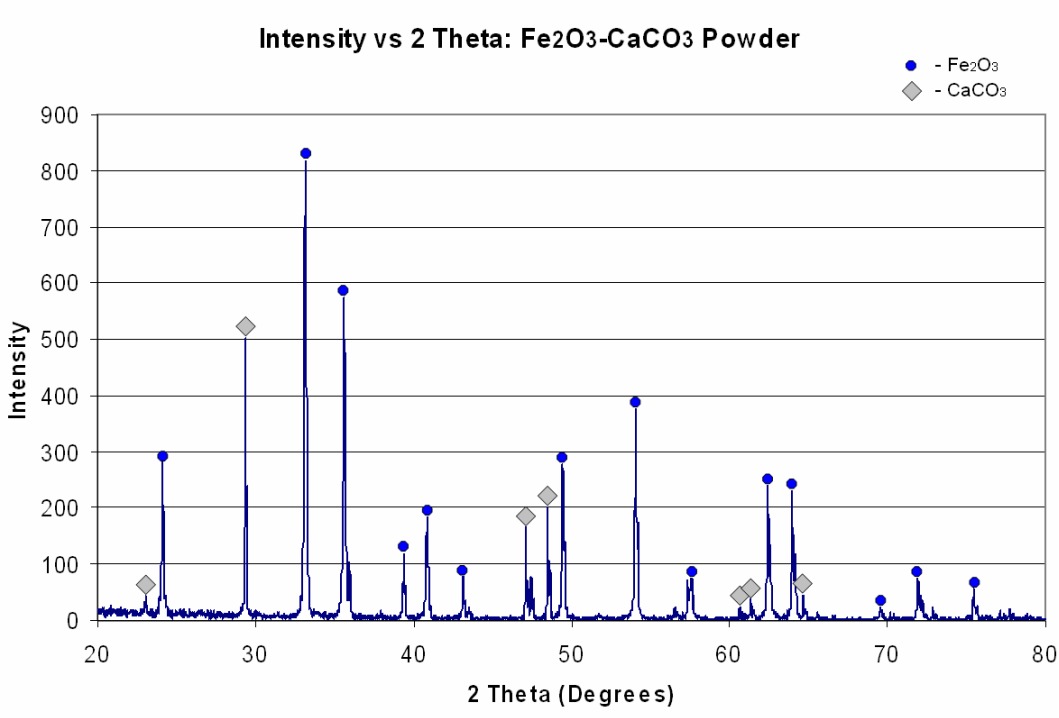

Figure 5: XRD pattern for the flux phase prior to calcination.

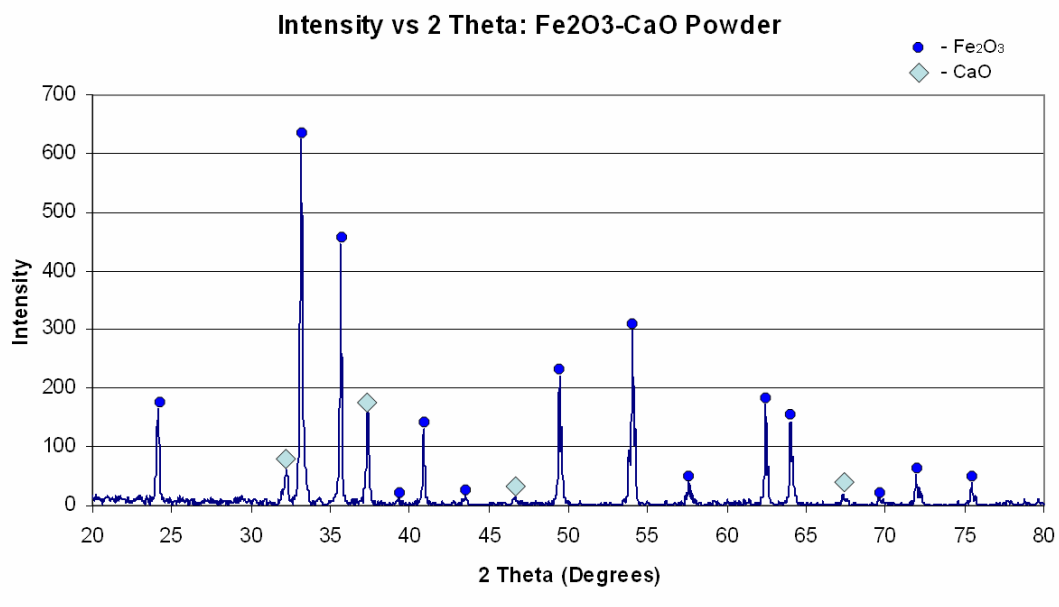

Figure 6: XRD pattern for the flux phase following calcination.

3.3 Sintering Studies

The processed TLP powders were used to produce pellets which were used in sintering studies. Sintering times varied from 1 to 6 hours and temperatures from 1100 to 1450°C.

The pellets microstructure was characterized with SEM to view the progression of the microstructure based on time and temperature. The microstructure changes significantly as sintering takes place (Figure 7).

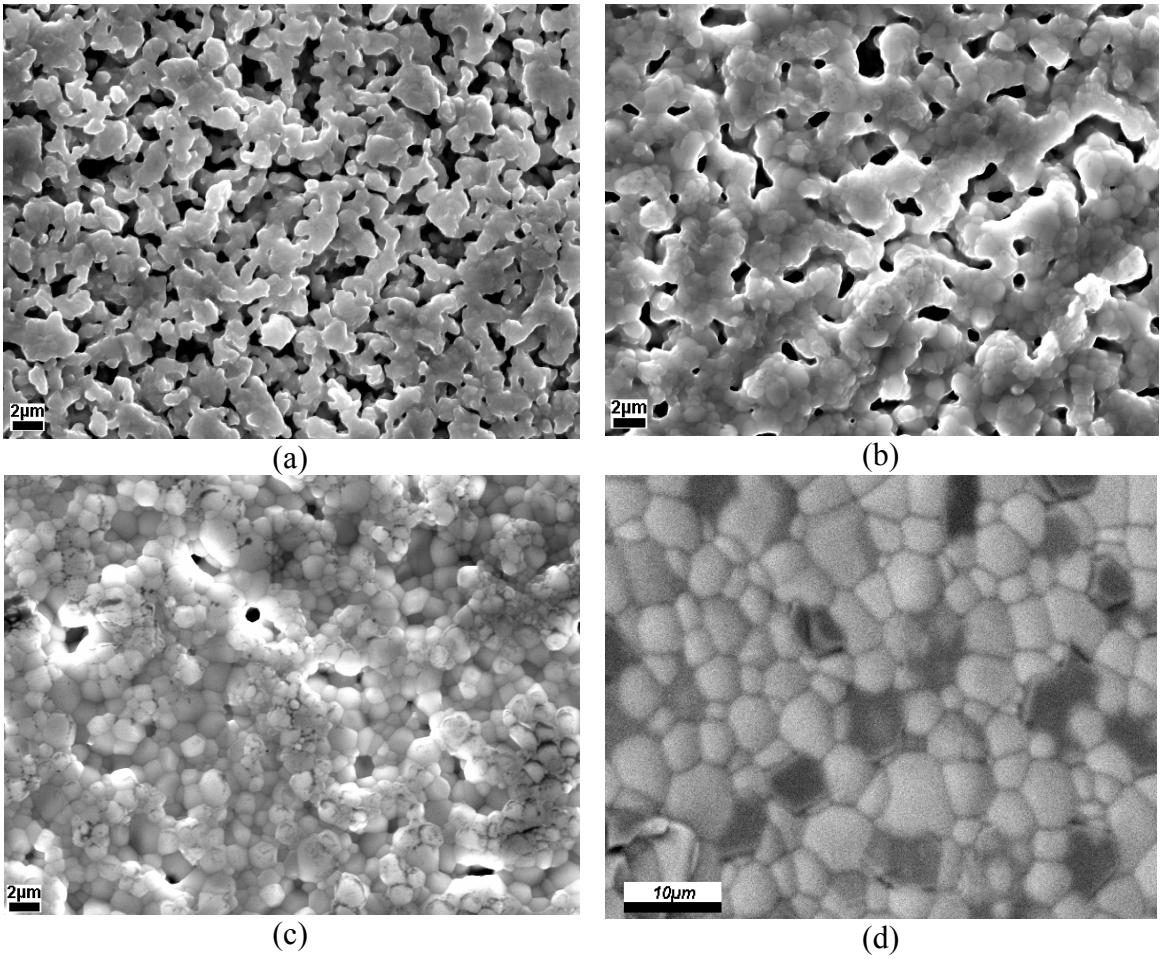

Figure 7: Microstructure of pellets made from the same batch of powder sintered at (a) 1200°C for 1 hour, (b) 1400°C for 1 hour, (c) 1400°C for 2 hours, and (d) 1450°C for 4 hours.

Increased time and temperatures lead to grain growth and the elimination of porosity. The difference between sintering for 1 hour at 1200°C as opposed to 1400°C is apparent (Figure 7(a,b). Less porosity and more pronounced grains exist at the higher temperature. An additional hour of sintering at 1400°C (Figure 7(c)) shows continued development of the microstructure. The majority of the porosity disappears with the additional time, and the grains become more pronounced.

X-Ray Diffraction (XRD) was used to verify the composition of the pellets. The XRD pattern from a monolithic specimen of $La_{0.9}Ca_{0.1}FeO_3$ provided by Ceramatec and from a pellet sintered for 4 hours and 1200°C are shown in Figures 8 and 9. The XRD patterns match.

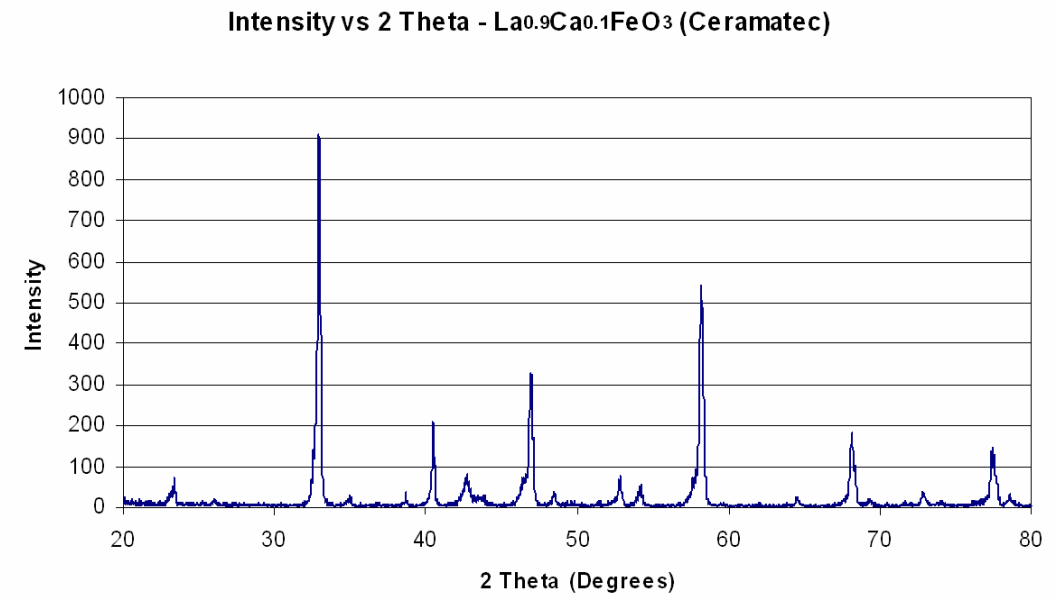

Figure 8: XRD pattern for monolithic $La_{0.9}Ca_{0.1}FeO_3$ provided by Ceramatec.

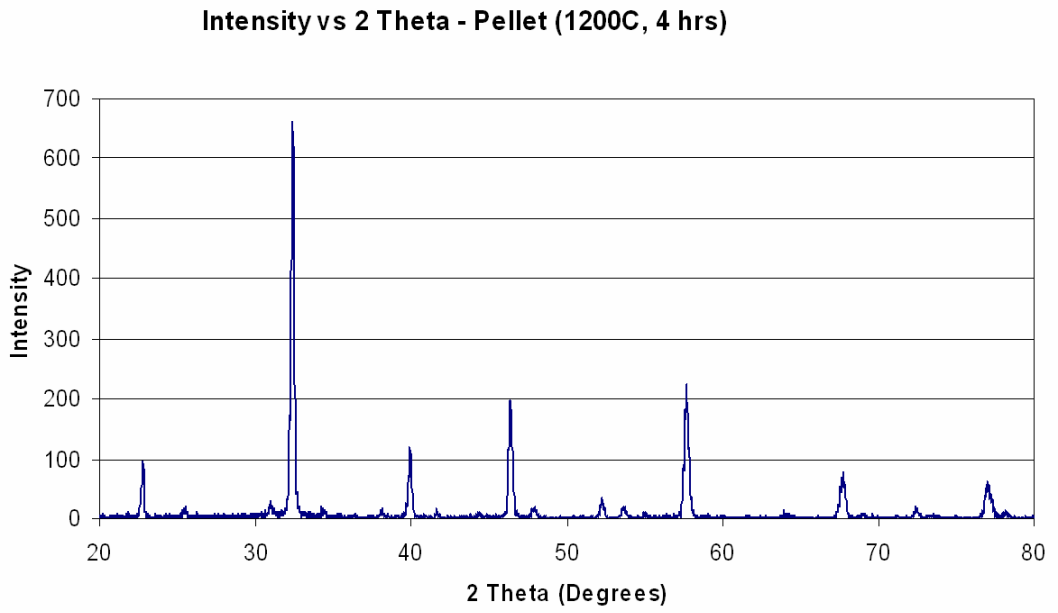

Figure 9: XRD pattern for a $La_{0.9}Ca_{0.1}FeO_3$ pellet sintered for 4 hours and 1200°C.

The reaction of the flux phase with the refractory phase to form the lanthanum calcium ferrite perovskite is an activated process so there is an activation energy associated with the reaction, and it will follow Arrhenius behavior. Arrhenius behavior is described by the Arrhenius equation which is:

$$\ln(k) = -\frac{E_a}{R}\left(\frac{1}{T}\right) + \ln(A)$$

By plotting the natural log of the peak intensity of several samples sintered at different temperatures for the same time, the activation energy can easily be found. XRD was performed on pellets sintered for 2 hours at various temperatures and the results were used.and used to find an activation energy for perovskite formation. The plot of the natural log of peak intensity as a function of $\frac{1}{T}$ is shown in Figure 10. The activation energy was found to be 108 kJ/mol.

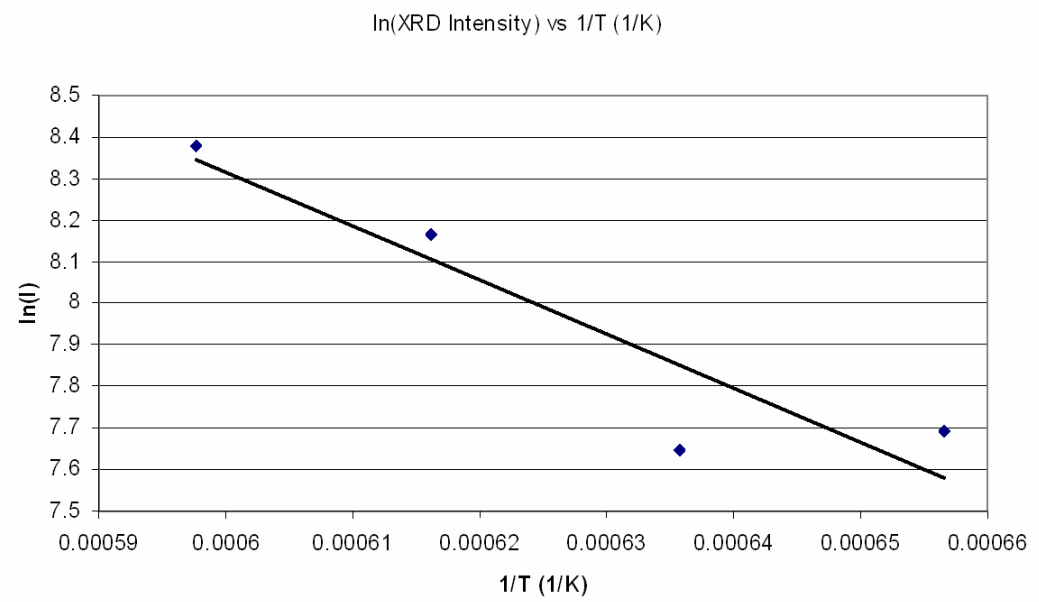

Figure 10: plot of the natural log of peak intensity versus $\frac{1}{T}$ for pellets sintered for 2 hours.

3.4 Wetting Behavior

Wetting behavior was studied by placing pieces of the flux phase on a polished $La_{0.9}Ca_{0.1}FeO_3$ substrate. The samples were heated above the flux's melting temperature for 4 hours and cooled to room temperature. The substrates were thoroughly wetted by the flux. SEM images of a wetted substrate are shown in Figure 11. The wetting angles were approximately zero, indicating that there is thorough wetting. This indicates that the liquid phase will fill the interfacial gap and surround the refractory phase during joining leading to a uniform, non-porous interface.

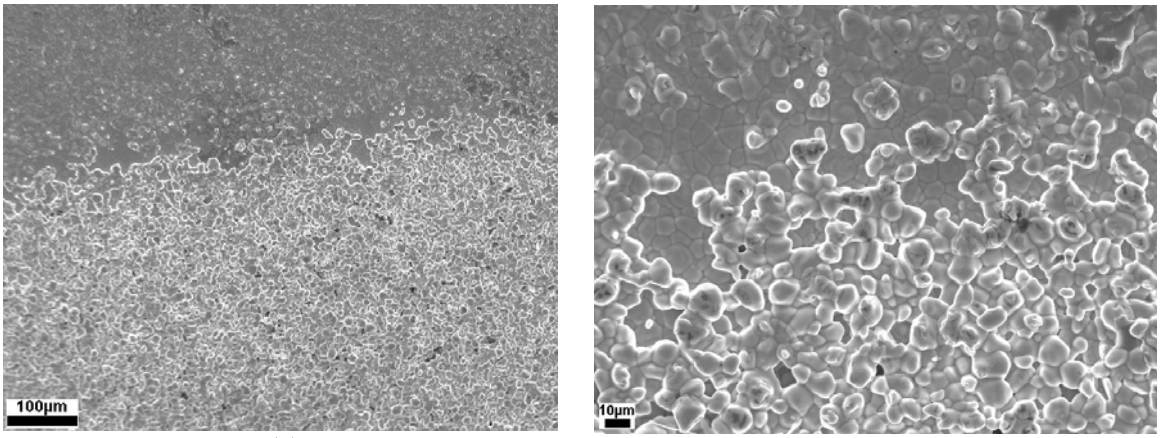

(a) (b)

Figure 11: Microstructure of a wetted substrate.

3.5 Joining

Numerous successful joints were fabricated from the tape cast pieces of $La_{0.9}Ca_{0.1}FeO_3$ over the course of this project. Joints were made from inks with nominal compositions of $La_{0.9}Ca_{0.1}FeO_3$, $La_{0.75}Ca_{0.25}FeO_3$, and $La_{0.9}Ca_{0.35}FeO_3$. All compositions produced satisfactory joints, even the $La_{0.9}Ca_{0.35}FeO_3$, showing the robustness of the process.

An optical micrograph of an early attempt at joining using a $La_{0.75}Ca_{0.25}FeO_3$ ink is shown in Figure 12. The joint is not particularly uniform, but was made from unmilled powders. What is interesting about this micrograph is not the joint but the crack running along the upper right section of the image. The crack has been partially repaired by the ink that has penetrated it. The TLP method can also be used to repair damaged lanthanum calcium ferrite specimens by applying the ink to a crack and heating to the joining temperature.

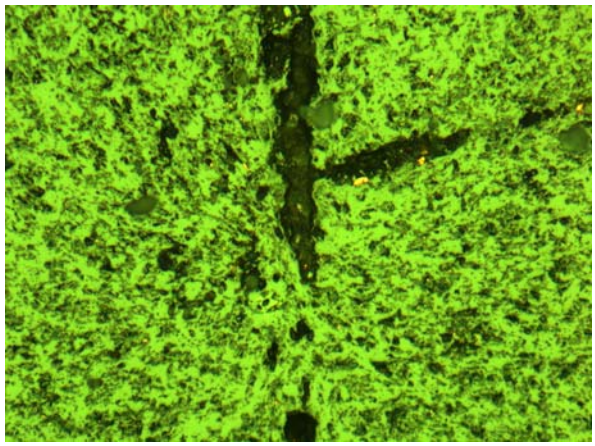

Figure 12: Optical micrograph of a joint made from a $La_{0.75}Ca_{0.25}FeO_3$ and unmilled powders.

An optical micrograph of another early joining attempt is shown in Figure 13. This joint was also made from unmilled powder. There are a significant number of voids present at the interface and uniformity is poor. Steps were taken in later joints to remedy these problems.

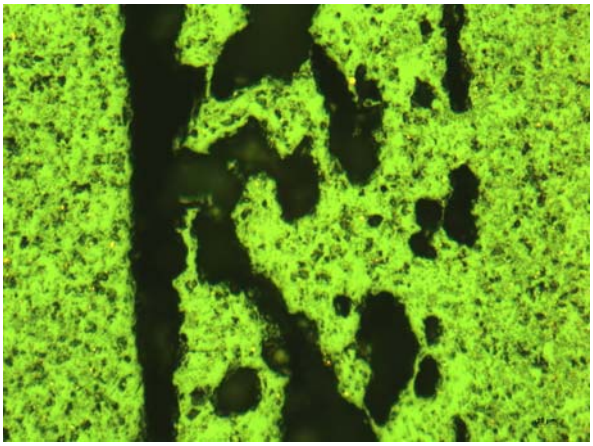

Figure 13: Optical micrograph of an early joining attempt made from a $La_{0.75}Ca_{0.25}FeO_3$ ink.

Some early joining attempts made use of an ink of nominal composition $La_{0.9}Ca_{0.35}FeO_3$. Although the composition is different from that of the parts that were joined, the joints were successful. Although the interfaces had voids as in Figures 12 and 13, the parts had successfully bonded, showing the robustness of the TLP process.

The problems in the joints shown in Figures 12 and 13 were remedied by changing the powder processing parameters. Powders were milled in isopropanol instead of dry, and the flux and refractory phases were mixed in isopropanol for longer times. Joints formed with the changed processing parameters are shown in Figures 14-16.

The effects of joint layer thickness were investigated. Using a $La_{0.9}Ca_{0.1}FeO_3$ ink, thin, medium, or thick layers of ink were applied to the parts. The thin joints were 1-5μm, the medium joints were 15-20μm, and the thick joints were 25-30 μm. Thickness was varied by applying additional or fewer layers of ink to the joint interface. These joints were heated to a temperature of 1350°C for 5 hours. All the joints were successful and had excellent mechanical integrity. The thicker joints had more voids present than the medium and thin joints (See Figure 14).Thinner joints were effectively free of any porosity.

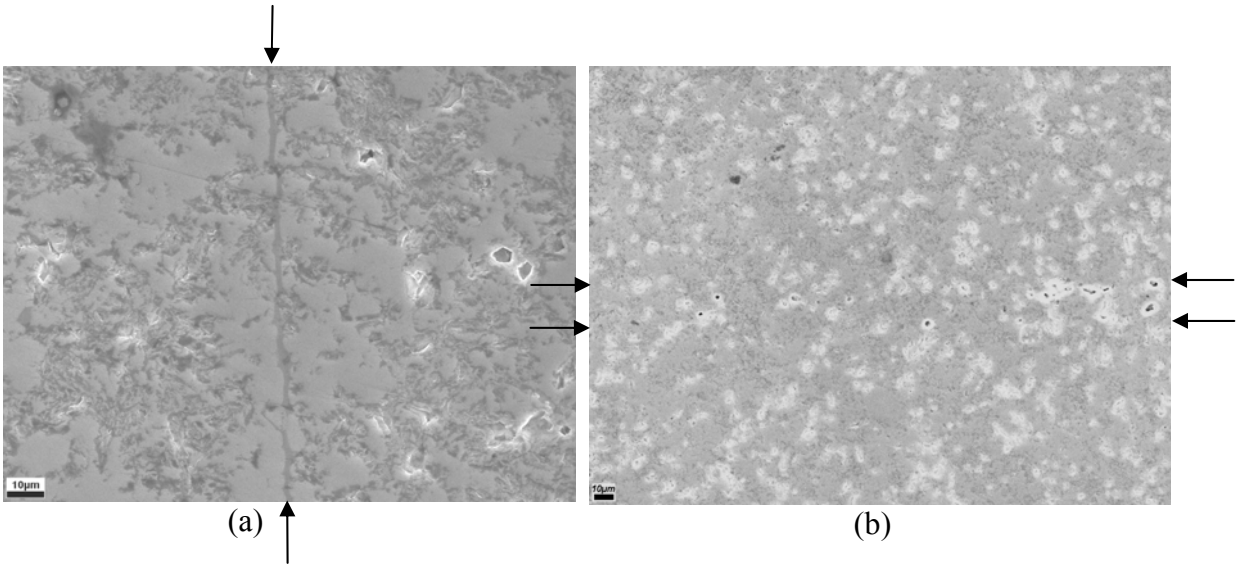

Figure 14: SEM images of (a) a thin joint and (b) a medium joint. The arrows indicate the joint interface.

Joining time and temperature also have significant effects on joint properties. The effects were studied by varying joining time and temperature. Joining times varied from 4-8 hours, and the joining temperatures varied from 1300°C-1450°C. None of these joints were broken by hand, although a force was applied to each before mounting on a diamond saw for cutting. A longer joining time resulted in better joints. The samples joined at 1300°C and 1350°C for 4 hours tended to break while being mounted on the diamond saw, while all others did not. This is because at the composition used, there is a limited amount of liquid phase developed, resulting in less wetting and slower joining. Figure 15(a) shows a joint that was heated to 1400°C for 4 hours. Figure 15(b) shows a joint that was heated to 1450°C for 4 hours.

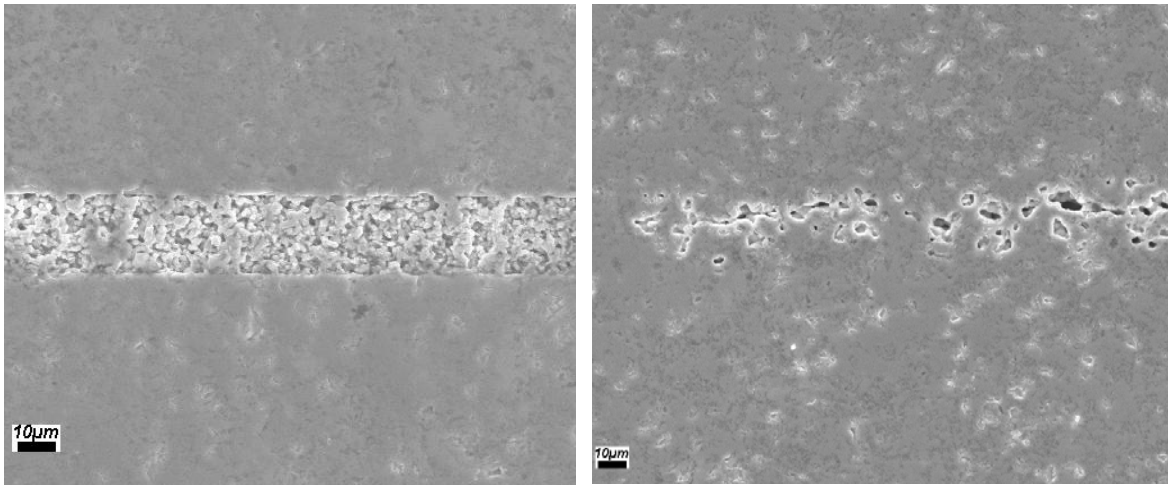

Figure 15 : SEM image of a joint formed for 4 hours at (a) 1400°C, and (b) 1450°C

The joint shown in Figure 15(a) is not ideal. If it had been heated longer the joint would be much less porous and difficult to distinguish from the joined pieces. From Figure

15(b) it is apparent that the higher temperature resulted in a better joint. There is much less porosity than the joint shown in the higher temperature joint and in places it is difficult to distinguish the joint from the joined parts. Figure 16(a) shows a joint that was heated to 1400°C for 8 hours. Comparing the joint in Figure 16(a) to the joint in Figure 15(a), it is apparent that the additional 4 hours at the joining temperature has removed almost all porosity and the joint has become almost indistinguishable from the joined parts. In places it is difficult to identify where the joint begins and ends, the only distinguishing features being several small pores.

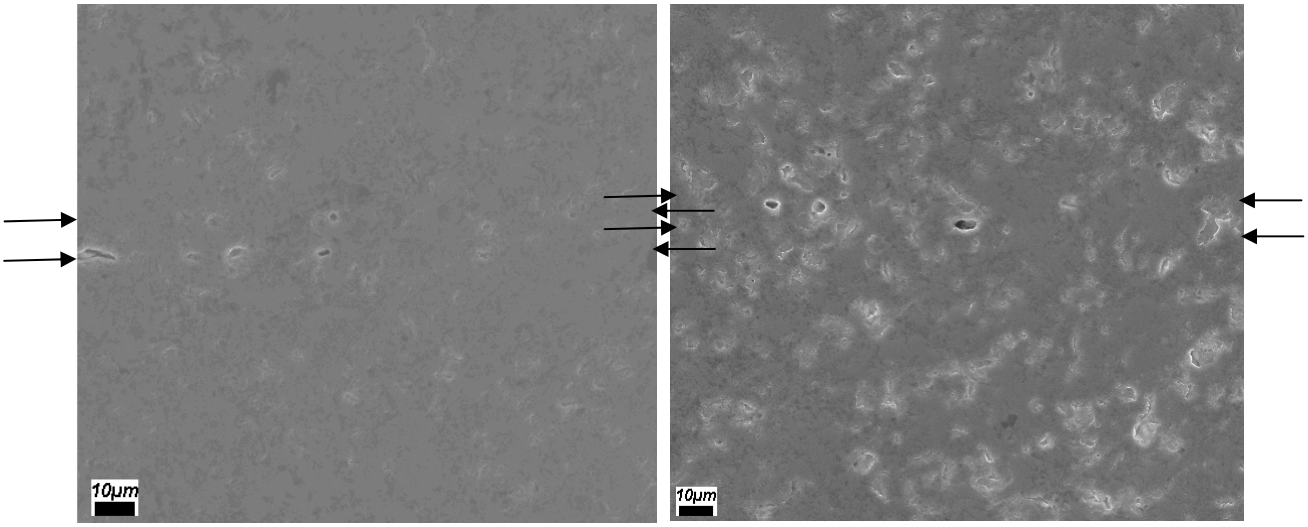

(a) (b)

Figure 16: SEM image of a joint formed for 8 hours at (a) 1400°C, and (b) 1450°C. The arrows indicate the joint interface.

The joints produced with this TLP method are ideal joints. While there are some pores along the joint interface, there is good joint uniformity and the joints are otherwise indistinguishable from the joined parts. It is also important to note that this method can make joints that are uniform on a large scale. It is not difficult to develop a uniform microstructure, but to develop joint uniformity on a macro scale is more difficult and the TLP method has accomplished this.

Extensive study on applying the method to the joining of dissimilar materials was not conducted but the preliminary results are promising. $La_{0.9}Ca_{0.1}FeO_3$ has been joined to alumina. Figure 17 shows $La_{0.9}Ca_{0.1}FeO_3$ that has joined with alumina boats.

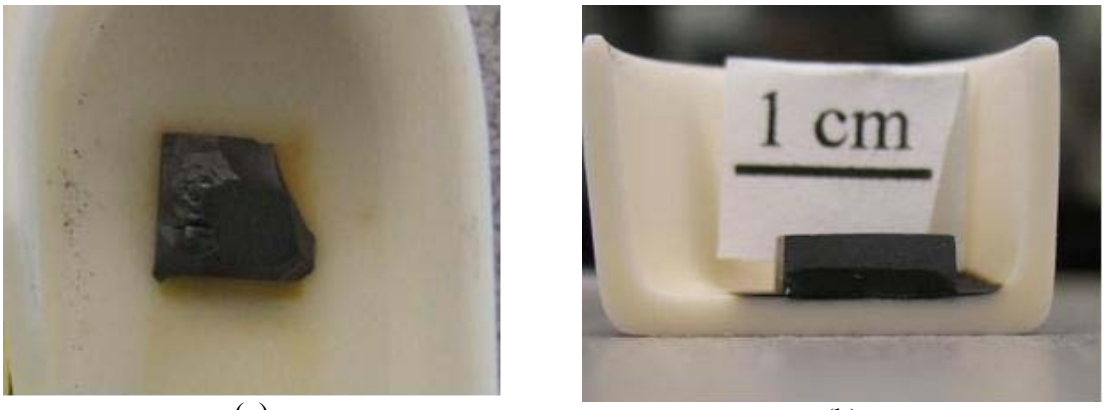

(a) (b)

Figure 18: $La_{0.9}Ca_{0.1}FeO_3$ joined with alumina boats. (a) Shows a sample which has been broken away from the surface it joined with, while (b) remains joined.

In Figure 17(a), the sample has been broken away from the alumina it joined with. The underside of the sample where it joined with the alumina boat is shown, and the broken pieces are still attached to the alumina (not shown). The sample shown in Figure 17(b) was not removed from the alumina boat. It was cut and the cross section polished. It is apparent that the TLP method that has been developed for the joining of ion transport membranes can be applied to joining dissimilar materials.

4. Summary and Conclusions

Many candidate systems have been identified where the TLP process could potentially be identified. A significant amount of research needs to be conducted to properly apply to method to other systems.

The wetting angle of the flux phase on a $La_{0.9}Ca_{0.1}FeO_3$ was approximately zero and the substrates are being thoroughly wetted. This indicates that the interfacial gaps will be filled with liquid phase and that the joint interface should be uniform and free of porosity.

Many successful, ideal joints were fabricated. The joint interface was the same material as the surrounding assembly, so they had the same properties and no thermal cycling stresses would be induced at the interfaces. The TLP process is cheap and easy to apply, and could easily be commercialized. One could fabricate tapes and supply them to companies who could use them to join their parts as needed.

Preliminary results show that the process can be used to join dissimilar materials. A significant amount of research needs to be conducted in the area to properly apply the process and determine what dissimilar materials could be joined satisfactorily.

References

1. D. P. Butt, R. A. Cutler, S. W. Rynders, M. F. Carolan, "Method of Joining Ion Transport Membrane materials Using a Partially or Fully-Transient Liquid Phase," U.S. Patent No. 7,011,898 (2006).
2. D. P. Butt, R. A. Cutler, S. W. Rynders, M. F. Carolan, "Method of Forming a Joint,"U.S. Patent No. 7,094,301 (2006).
3. D. P. Butt, R. A. Cutler, S. W. Rynders, and M. F. Carolan, "Metallic Oxide Interlayer Compositions for Joining of Sintered Ceramics to Form a Composite Structure with Heat Treatment at Below Sintering Temperatures," U.S. Patent Application 2004182306, Filed 2004.
4. D. P. Butt, R. A. Cutler, S. W. Rynders, and M. F. Carolan, "Method for Joining Multicomponent Oxide Materials Using a Partially or Fully Transient Liquid Phase of Low-Melted Ceramics," U. S. Patent Application No. 2004185236, Filed 2004.
5. D. P. Butt, R. A. Cutler, S. W. Rynders, and M. F. Carolan, "Metallic Oxide Interlayer Compositions for Joining of Sintered Ceramics to Form a Composite Structure with Heat Treatment at Below Sintering Temperature," U. S. Patent Application No. 2004182306, Filed 2004.
6. B. Phillips and A. Muan, "Phase Equilibria in the System CaO-IronOxide in Air and at 1 atm O_2 Pressure," *J. Am. Ceram. Soc.*, 41 (9) (1958), 445-454.
7. R. U. Vaidya, A. H. Bartlett, H. Kung, and D. P. Butt, "Joining of $MoSi_2$ to Itself and Reaction With Aluminium Interlayers," *Journal of Materials Science Letters*, 17 (1998), 777-780.
8. R. N. Lumley and G. B. Schaffer, "The Effect of Solubility and Particle Size on Liquid Phase Sintering," *Scripta Materiala*, 35 (5) (1996), 589-595.
9. S. D. Conzone, D. P. Butt, and A. H. Bartlett, "Joining $MoSi_2$ to 316L Stainless Steel," *J. Mater. Sci*., 32 (1997), 3369-3374.
10. B. G. Ravi abd R. Chaim, "Joining of ZrO_2-4.5 wt% Y_2O_3 (Y-TZP) Ceramics Using Nanocrystalline Tape Cast Interlayers," *J. Mater. Sci*., 37 (2002) 813-818.
11. S. D. Peeves, M. Paulasto, G. Ceccone, and V. Stamos, "The Reactive Route to Ceramic Joining: Fabrication, Interfacial Chemistry and Joint Properties," *Acta Mater*., 46 (7) (1998), 2407-2414.
12. M. R. Locatelli, B. J. Dalgleish, K. Nakashima, A. P. Tomsia, and A. M Glaeser, "New Approaches to Joining Ceramics for High-Temperature Applications," *Ceramics International*, 23 (1997) 313-322.
13. L. A. Chick, J. Liu, J. W. Stevenson, T. R. Armstrong, D. E. McCready, G. D. Maupin, G. W. Coffey, and C. A. Coyle, "Phase Transitions and Transient Liquid-Phase Sintering in Calcium-Substituted Lanthanum Chromite," *J. Am. Ceram. Soc*., 80 (8) (1997) 2109-2120.
14. Y. Zhou, W. F. Gale, and T. H. North, "Modelling of Transient Liquid Phase Bonding," *International Materials Review*, 40 (5) (1995) 181-196.

15. D. Treheux, P. Lourdin, B. Mbongo, and D. Juve, "Metal-Ceramic Solid State Bonding: Mechanisms and Mechanics," *Scripta Metallurgica et Materialia*, 31 (8) (1994) 1055-1060.

16. C. Hu and T. N. Baker, "An Analysis of the Capillary Force and Optimum Liquid Volume in a Transient Liquid Phase Sintering Process," *Materials Science and Engineering*, A190 (1995) 125-129.

17. W. F Gale and E. R. Wallach, "Microstructural Development in Transient Liquid-Phase Bonding," Metallurgical Transactions, 22A (1991) 2451-2457.

18. J. Li, "Investigation of Orthorhombic Perovskite $La_{1-x}Ca_{xFeO3-v}$ $(0 \leq x \leq 0.5)$," *Physica Scripta*, 45 (1992) 62-64.

Appendix A – Candidate Systems

How to Read:

SrO-B_2O_3 } Indicates System

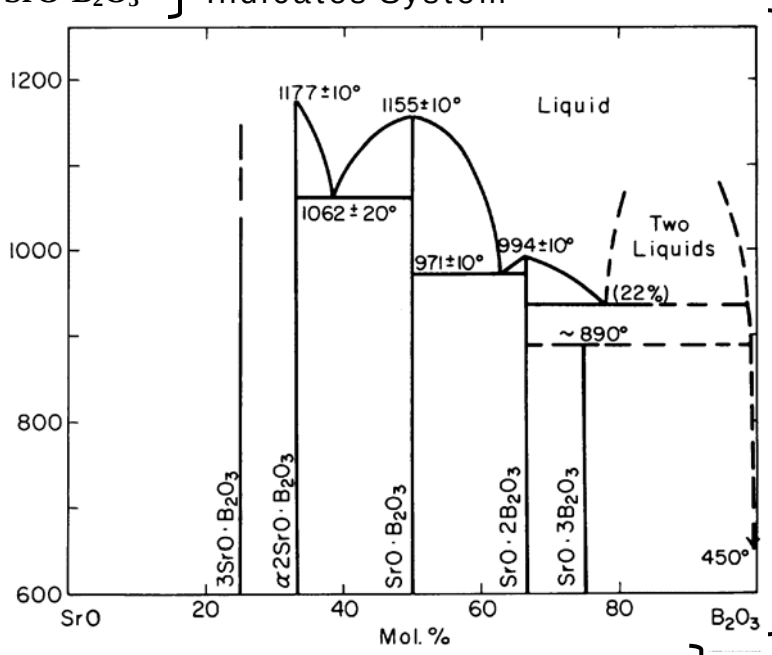

Phase diagram associated with system

SrO-B_2O_3 phase diagram. PEDv2.1 Diagram 2333. } PEDv2.1 diagram number

H. Witzmann, G. Herzog, "Luminescence-optical behavior of alkaline earth borate luminophors", *Z. Phys. Chem. (Leipzig)*, **225** [3-4] 197-208 (1964). } Indicates diagram source

---

The line separates systems

SrO-B_2O_3

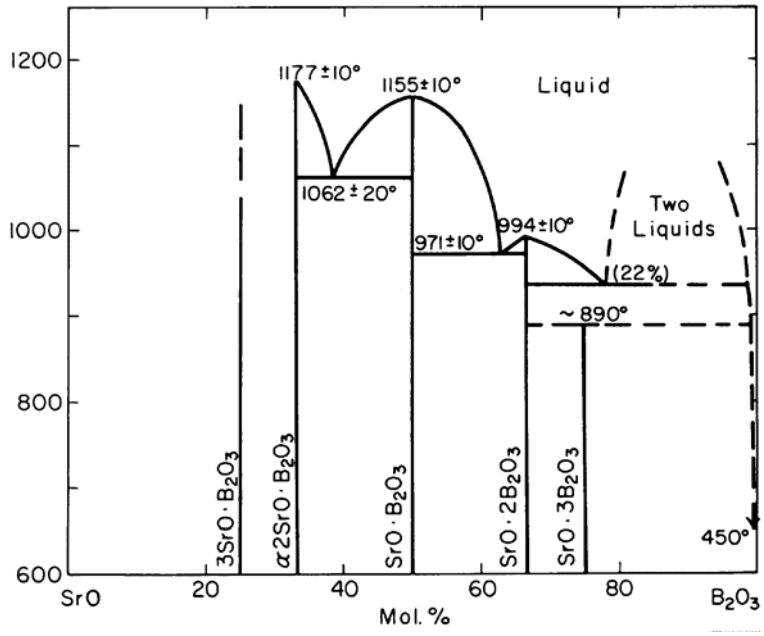

SrO-B_2O_3 phase diagram. PEDv2.1 Diagram 2333.

H. Witzmann, G. Herzog, "Luminescence-optical behavior of alkaline earth borate luminophors", *Z. Phys. Chem. (Leipzig)*, **225** [3-4] 197-208 (1964).

SrO-BaO-B_2O_3

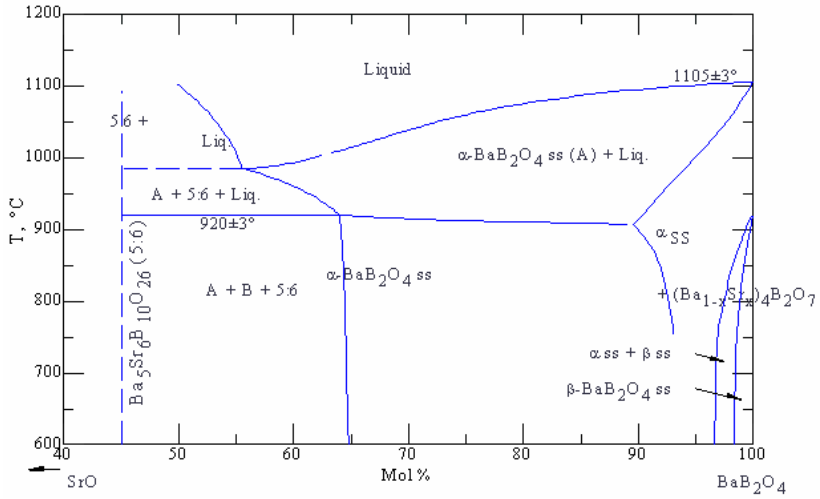

SrO-BaO-B_2O_3 phase diagram. PEDv2.1 Diagram 92-029.

G. Wang, Q. Z. Huang, J. Liang, "Phase equilibrium relation in barium borate (BaB_2O_4)-strontium borate (SrB_2O_4)-strontium oxide binary sections", *Huaxue Xuebao*, **42** 503-508 (1984).

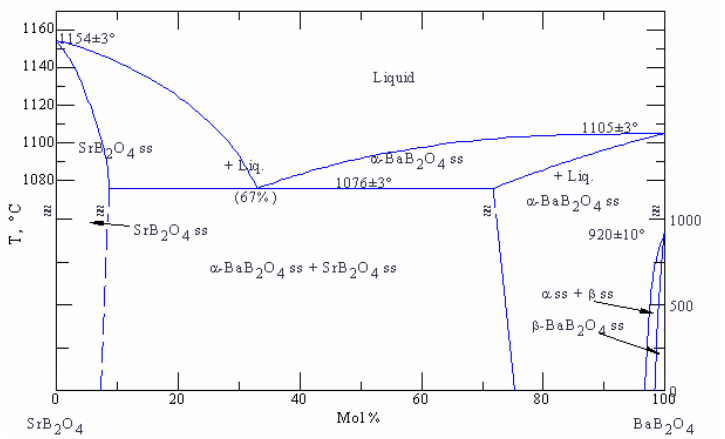

SrO-BaO-B_2O_3 phase diagram. PEDv2.1 Diagram 92-030.

G. Wang, Q. Z. Huang, J. Liang, "Phase equilibrium relation in barium borate (BaB_2O_4)-strontium borate (SrB_2O_4)-strontium oxide binary sections", *Huaxue Xuebao*, **42** 503-508 (1984).

SrO-BaO-GeO_2

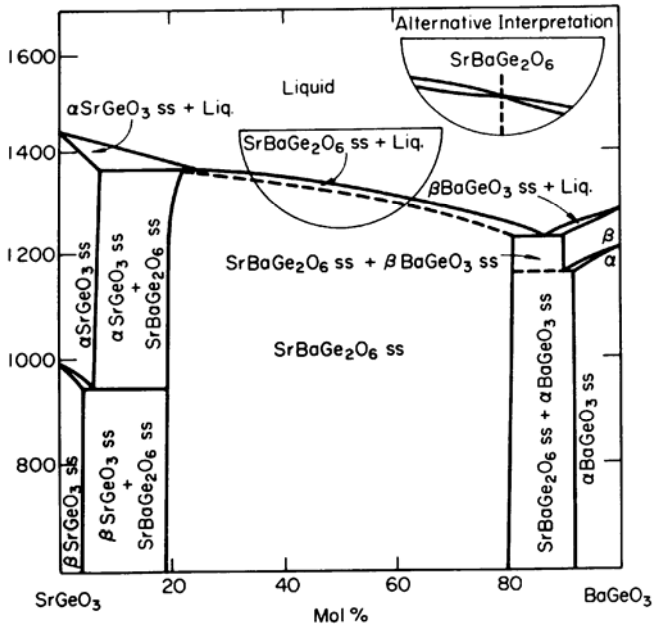

SrO-BaO-GeO_2 phase diagram. PEDv2.1 Diagram 5364.

R.G. Grebenshchikov, A. K. Shirvinskaya, V. N. Parfenenkov, "$BaGeO_3$ systems", *Izv. Akad. Nauk SSSR, Neorg. Mater.*, **6** [2] 323-326 (1970).

SrO-BeO

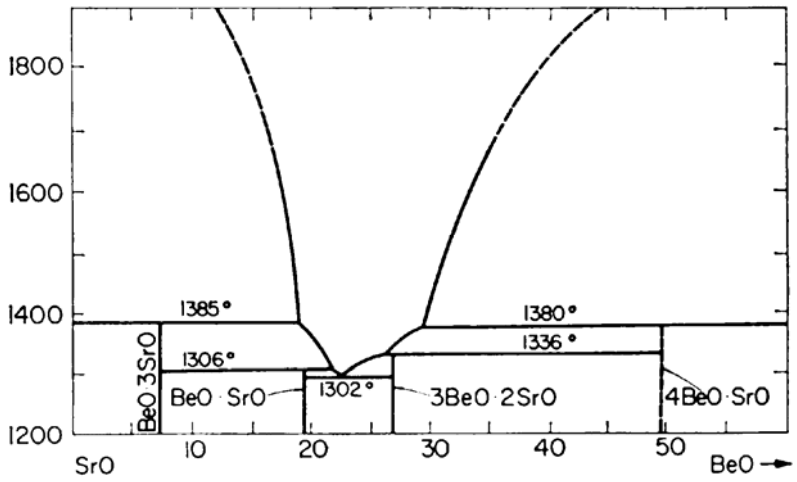

SrO-BeO phase diagram. PEDv2.1 Diagram 0217.

A. Auriol, G. Hauser, J. G. Wurm; private communication, 1961.

SrO-Bi_2O_3

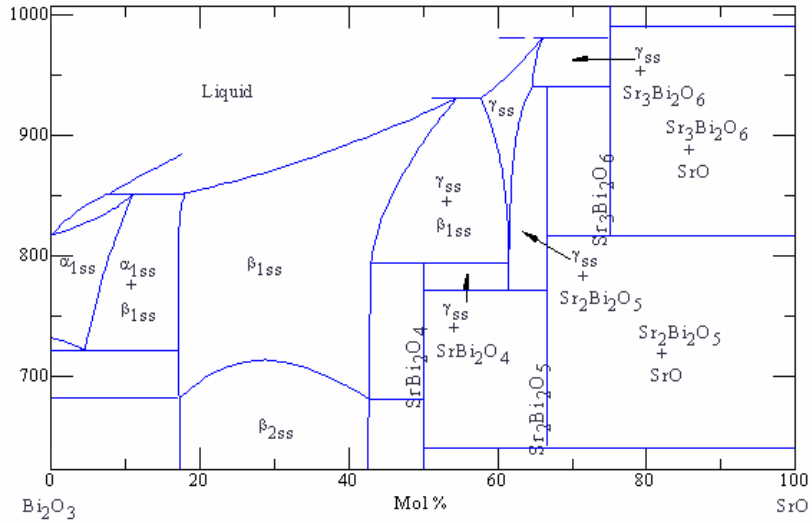

SrO-Bi_2O_3 phase diagram. PEDv2.1 Diagram 6428.

R. Guillermo, P. Cnflant, J. C. Boivin, D. J. Thomas, "Diagram of the solid phases of the bismuth trioxide-strontium oxide system", *Rev. Chim, Miner.*, **15** [2] 153-159 (1978).

SrO-Bi_2O_3-CaO-CuO-PbO

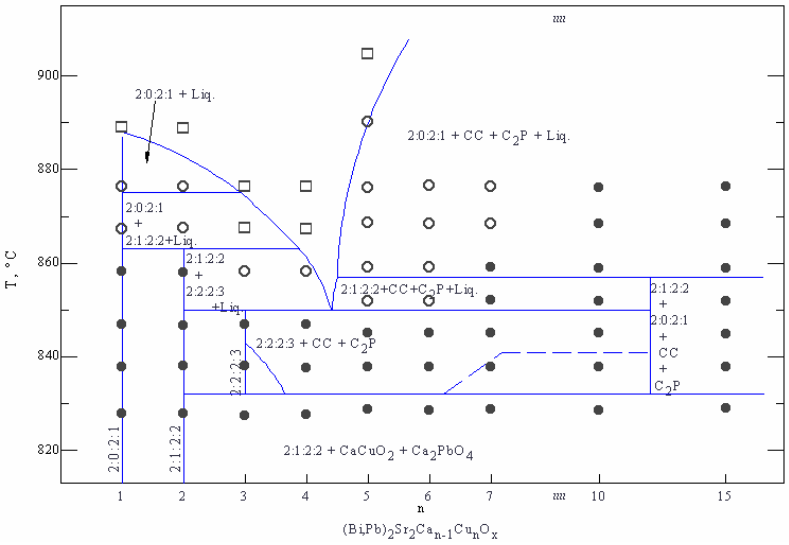

SrO-Bi_2O_3-CaO-CuO-PbO phase diagram. PEDv2.1 Diagram S-231.

P. Strobel, T. Fournier, "Phase diagram studies in the Bi(Pb)-Sr-Ca-Cu-O system", *J. Less-Common Met.*, **164-165** [1-2] 519-525 (1990).

SrO-Bi_2O_3-CaO-CuO

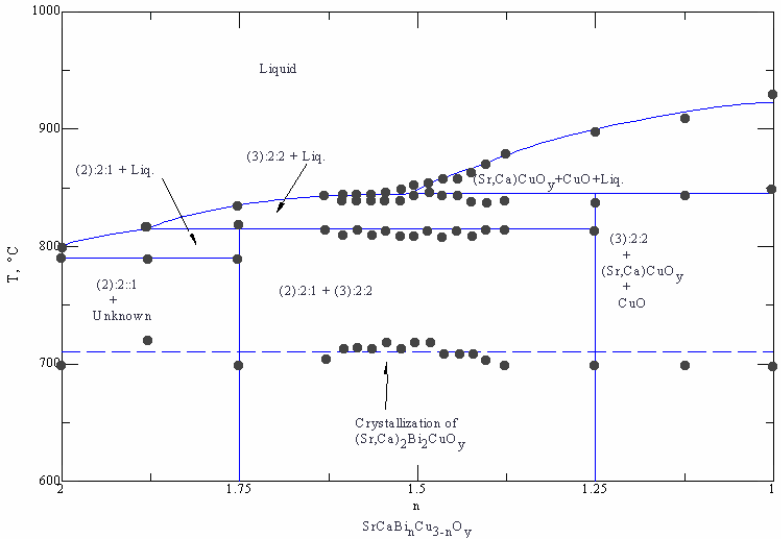

SrO-Bi_2O_3-CaO-CuO phase diagram. PEDv2.1 Diagram S-220.

K. Tomomatsu, A. Kurosaka, H. Tominaga, T. Takayama, O. Fukada, H. Osanai, "Phase diagram of bismuth strontium calcium copper oxide ($Bi_nSrCaCu_{3-n}O_y$) on line $1 \leq n \leq 2$", *Appl. Phys. Lett.*, **55** [3] 298-300 (1989).

SrO-CaO-GeO_2

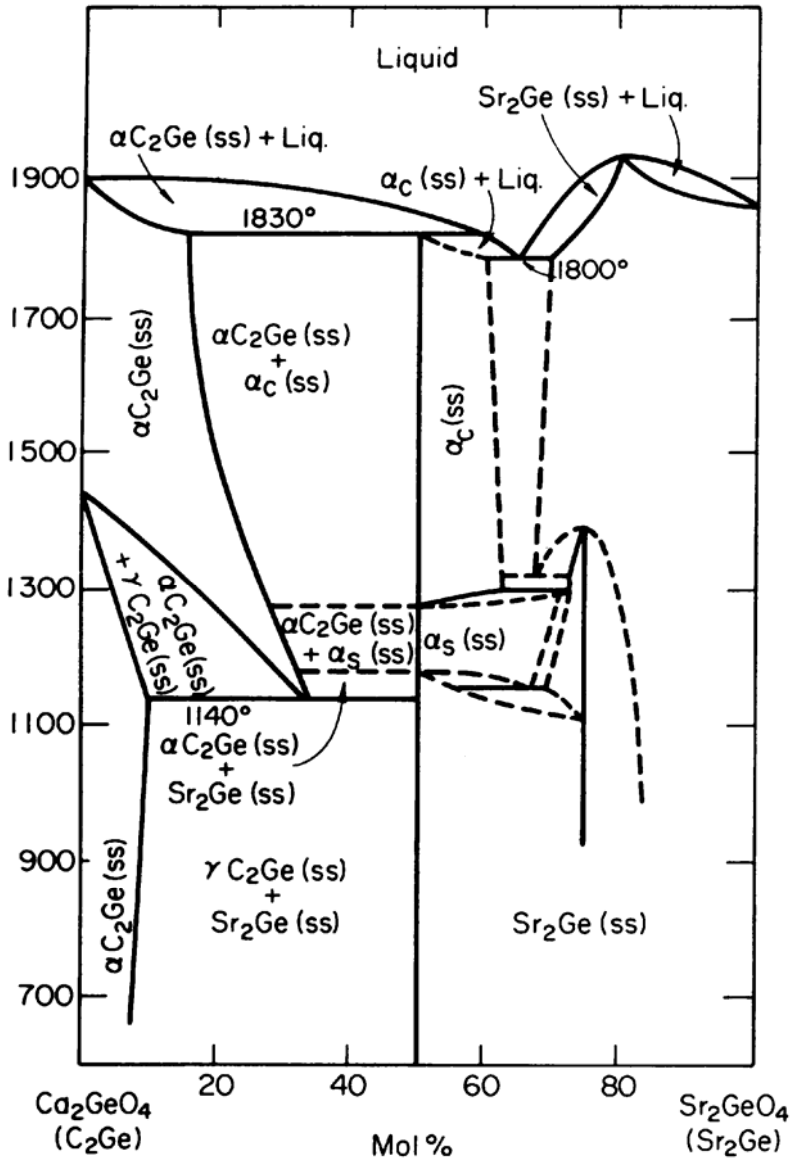

Figure SrO-CaO-GeO_2 phase diagram. PEDv2.1 Diagram 5384.

R. G. Grebenshchikov, V. I. Shitova, "Calcium germanium oxide-strontium germanium oxide (Ca_2GeO_4-Sr_2GeO_4) system", *Dokl. Akad. Nauk SSSR*, **218** [1] 96-99 (1974).

SrO-CaO-V_2O_5

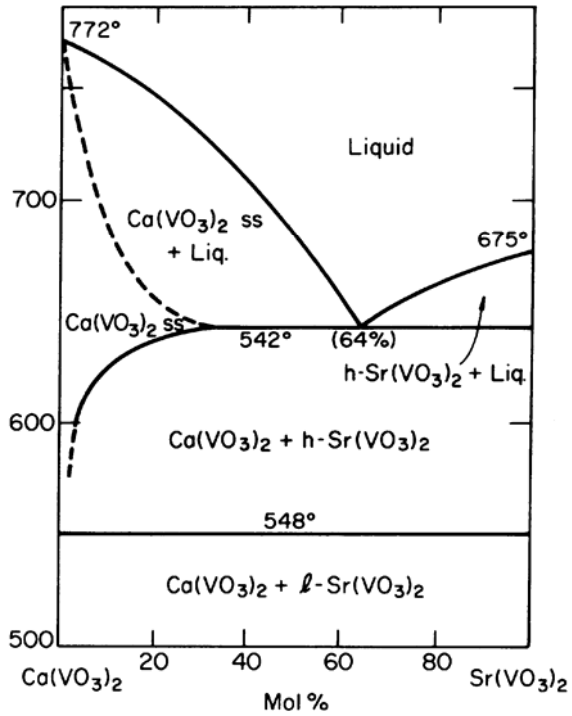

SrO-CaO-V_2O_5 phase diagram. PEDv2.1 Diagram 5385.

M. P. Glazyrin, A. A. Ivakin, S. I. Alyamovskii, "Phase diagrams of magnesium metavanadate-potassium metavanadate, magnesium metavanadate-strontium metavanadate, and calcium metavanadate-strontium metavanadate pseudobinary systems", *Zh. Neorg. Khim.*, **20** [4] 1081-1084 (1975).

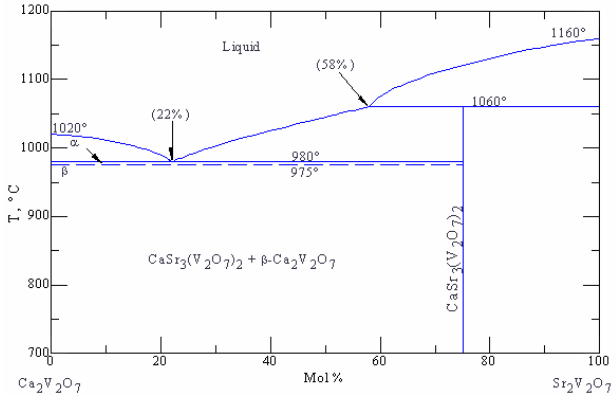

SrO-CaO-V_2O_5 phase diagram. PEDv2.1 Diagram 91-061.

A. A. Fotiev, V. D. Zhuravlev, V. P. Zhukov, "Phase diagrams of the strontium vanadate ($Sr_2V_2O_7$)- $M_2V_2O_7$ and barium vanadate ($Ba_2V_2O_7$)- $M_2V_2O_7$ systems where M = Ca, Cd", *Zh. Neorg. Khim.*, **27** [2] 482-484 (1982).

SrO-CdO-V_2O_5

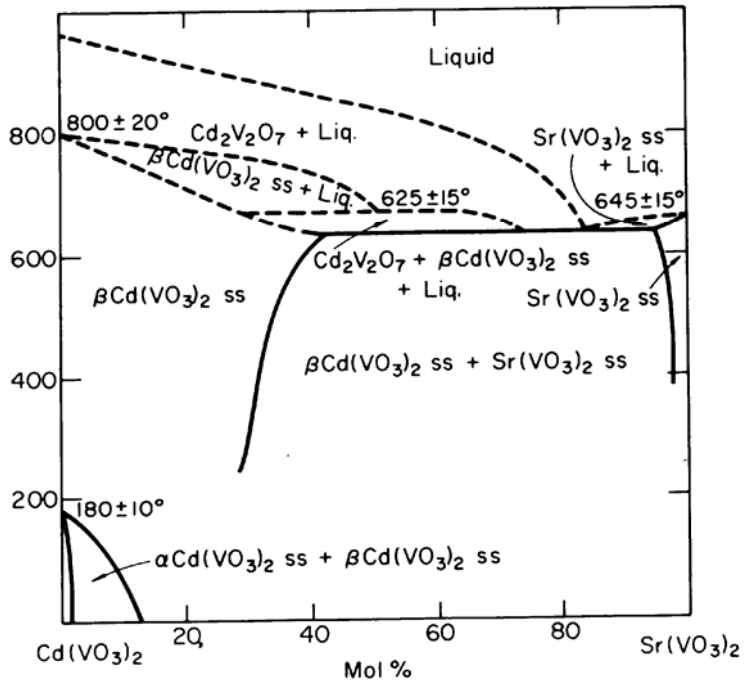

SrO-CdO-V_2O_5 phase diagram. PEDv2.1 Diagram 5398.

J. J. Brown, Jr., "Phase equilibrium in the system strontium oxide-calcium oxide-vanadium pentoxide", *J. Am. Ceram. Soc.*, **55** [10] 500-503 (1972).

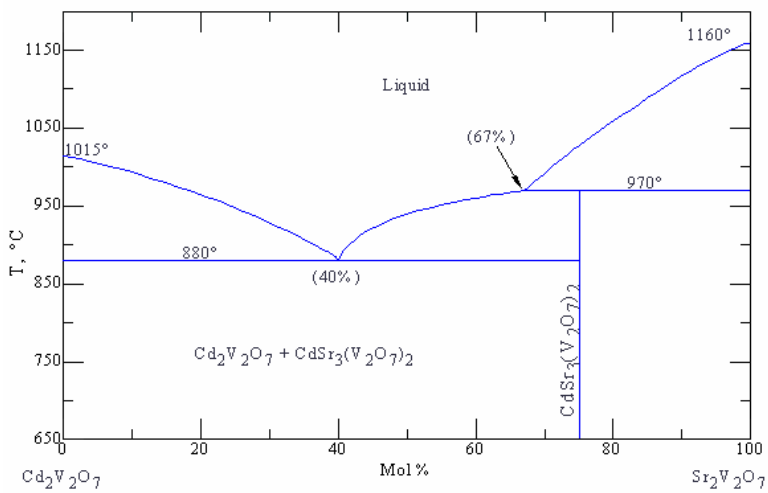

SrO-CdO-V_2O_5 phase diagram. PEDv2.1 Diagram 91-062. [12]

A. A. Fotiev, V. D. Zhuravlev, V. P. Zhukov, "Phase diagrams of the strontium vanadate ($Sr_2V_2O_7$)- $M_2V_2O_7$ and barium vanadate ($Ba_2V_2O_7$)- $M_2V_2O_7$ systems where M = Ca, Cd", *Zh. Neorg. Khim.*, **27** [2] 482-484 (1982).

SrO-CuO

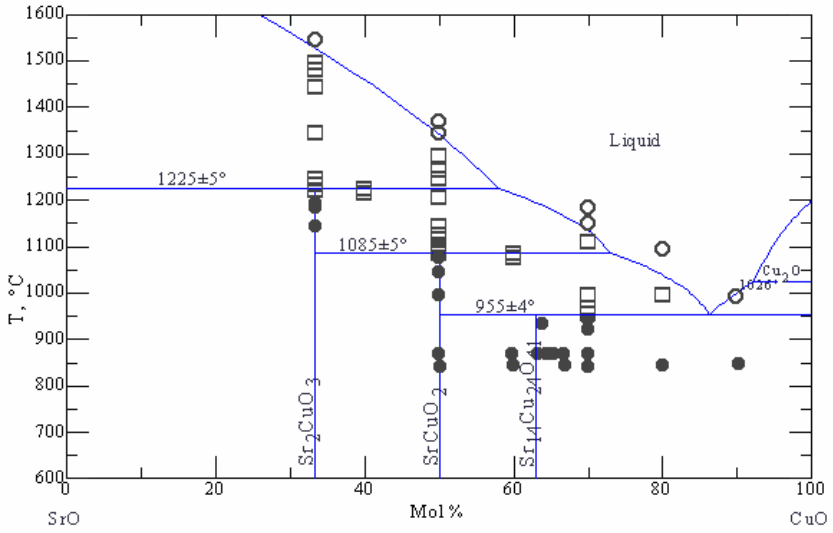

SrO-CuO phase diagram. PEDv2.1 Diagram S-053.

R. S. Roth, C. J. Rawn, J. D. Whitler, C. K. Chiang, and W. K. Wong-Ng, *J. Am. Ceram. Soc.*, **72** [3] 395-399 (1989).

SrO-CuO-La_2O_3

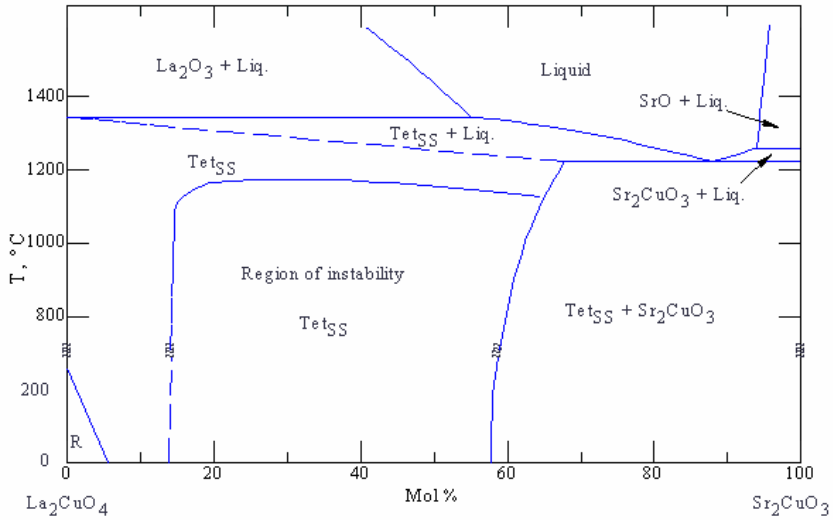

SrO-CuO-La_2O_3 phase diagram. PEDv2.1 Diagram S-156.

M. A. Petrova, A. S. Novikova, V. F. Popova, R. G. Gerbenshchikov, "Phase relationships in the system La_2CuO_4-Sr_2CuO_3", *Sverkhprovodimost: Fiz., Khim., Tekh.,* **3** [11] 2581-2586 (1990).

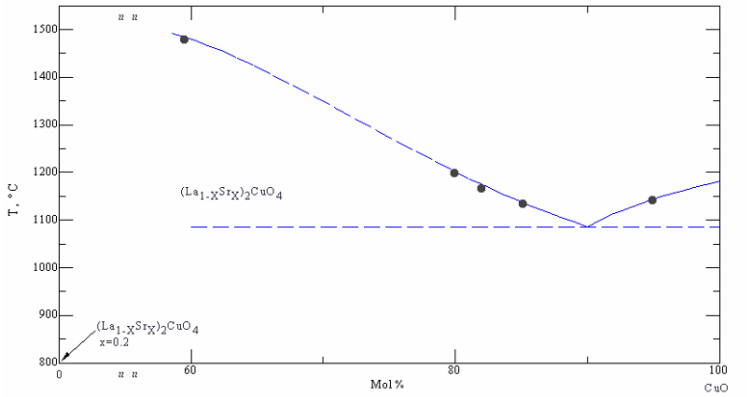

$(La_{1-x}Sr_x)_2CuO_4$-CuO phase diagram. PEDv2.1 Diagram S-151.

Y. Hidaka, Y. Enomoto, M. Suzuki, M. Oda, T. Murakami, "Single Crystal Growth of $(La_{1-x}A_x)_2CuO_4$(A=Ba or Sr) and $Ba_2YCu_3O_{7-y}$," *J. Cryst. Growth*, **85** [4] 581-584 (1987).

SrO-MgO-V_2O_5

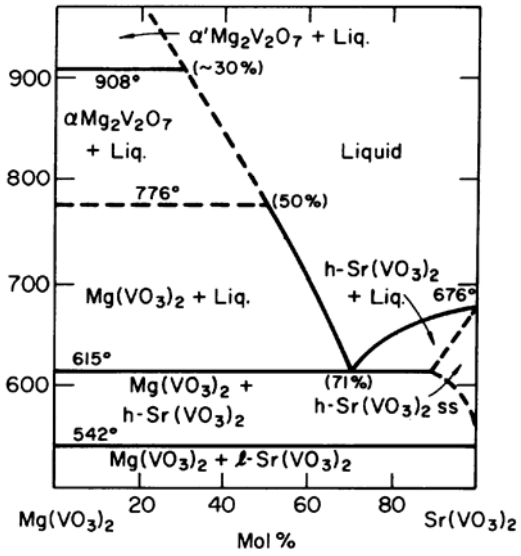

SrO-MgO-V_2O_5 phase diagram. PEDv2.1 Diagram 5411.

M. P. Glazyrin, A. A. Ivakin, S. I. Alyamovskii, "Phase diagrams of magnesium metavanadate-potassium metavanadate, magnesium metavanadate-strontium metavanadate, and calcium metavanadate-strontium metavanadate pseudobinary systems", *Zh. Neorg. Khim.*, **20** [4] 1081-1084 (1975).

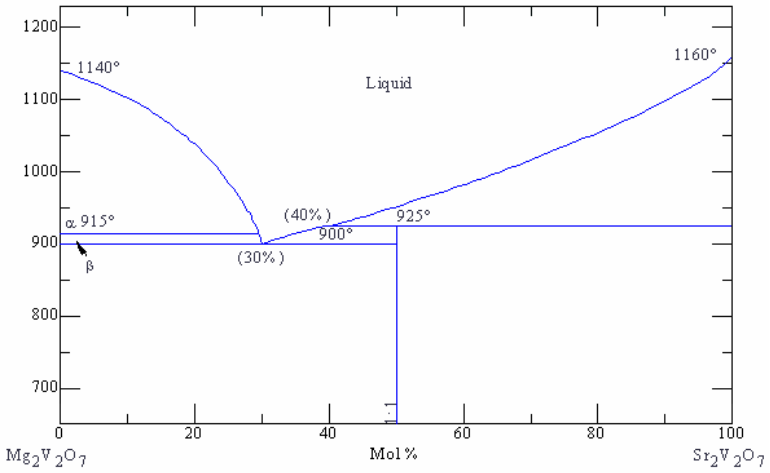

SrO-MgO-V_2O_5 phase diagram. PEDv2.1 Diagram 6740.

V. D. Zhuravlev, A. A. Fotiev, V. P. Zhukov, L. V. Kristallov, "Study of the magnesium vanadate ($Mg_2V_2O_7$)-strontium vanadate ($Sr_2V_2O_7$) and zinc vanadate ($Zn_2V_2O_7$)-$M_2V_2O_7$ systems (M = Mg, Ca, Sr)", *Zh. Neorg. Khim.*, **27** [4] 1018-1021 (1982).

SrO-Ga_2O_3

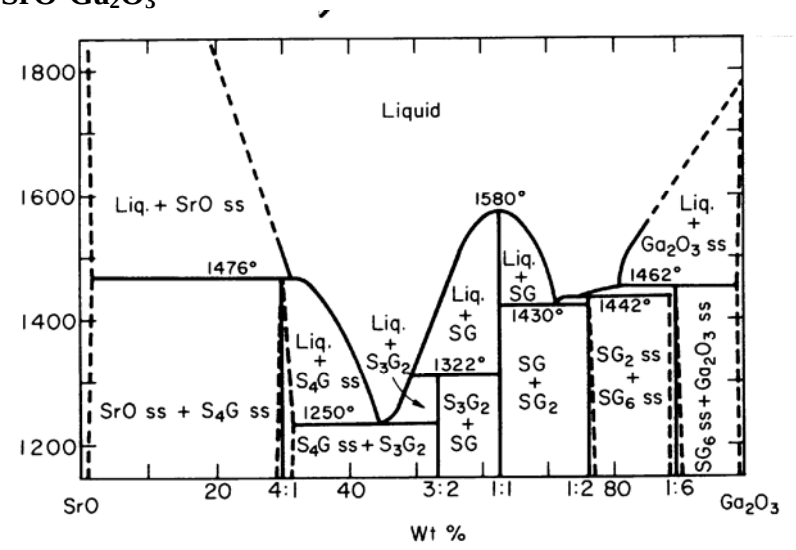

SrO-Ga_2O_3 phase diagram. PEDv2.1 Diagram 4359.

P. Batti, G. Sloccari, "Phase diagram of the strontium oxide-gallium(III) oxide system", *Ann. Chim. (Rome)*, **59** [2] 155-162 (1969).

SrO-MoO_3

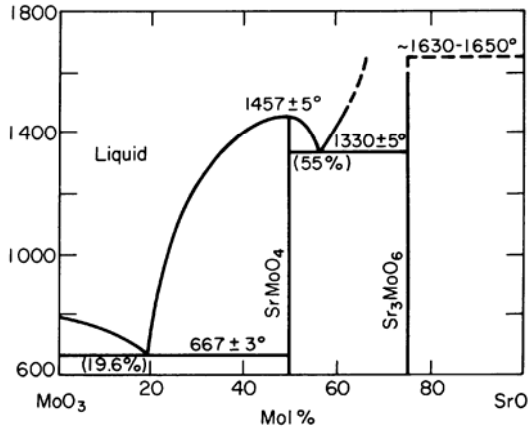

$SrO-MoO_3$ phase diagram. PEDv2.1 Diagram 5184.

V. M. Zhukovitskii, T. M. Yanushkevich, T. F. Tel'nykh, "Phase diagram of the molybdenum trioxide-strontium oxide system", *Zh. Neorg. Khim.*, **17** [10] 1481-1483 (1972).

SrO-MoO_3-La_2O_3

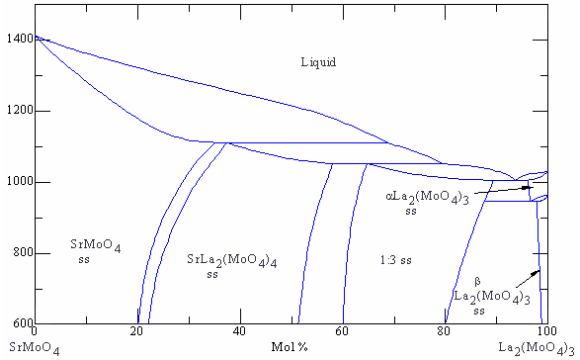

$SrO-MoO_3-La_2O_3$ phase diagram. PEDv2.1 Diagram 6804.

V. P. Sirotinkin, A. A. Evdokimov, V. K. Trunov, "Phase diagrams of $AMoO_4$-$La_2(MoO_4)_3$ systems (A = calcium-barium, lead)", *Zh. Neorg. Khim.*, **26** [7] 1889-1893 (1981).

SrO-MoO_3-Sm_2O_3

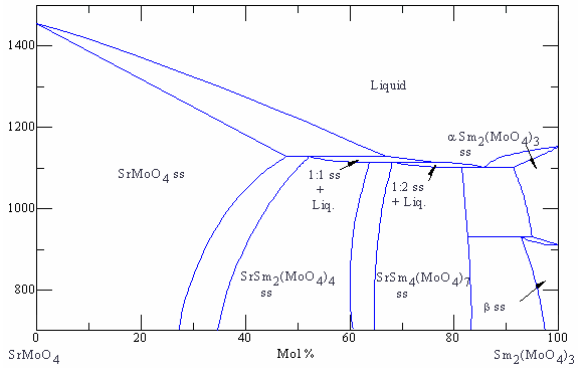

SrO-MoO_3-Sm_2O_3 phase diagram. PEDv2.1 Diagram 6807.

V. V. Vakulyuk, A. A. Evdokimov, T. A. Berezina, "Phase relations in calcium (strontium) molybdate-lanthanide molybdate (Ca(Sr)MoO_4-$Ln_2(MoO_4)_3$) systems, where Ln = praseodymium to lutetium", *Zh. Neorg. Khim.*, **27** [7] 1812-1814 (1982).

SrO-WO_3

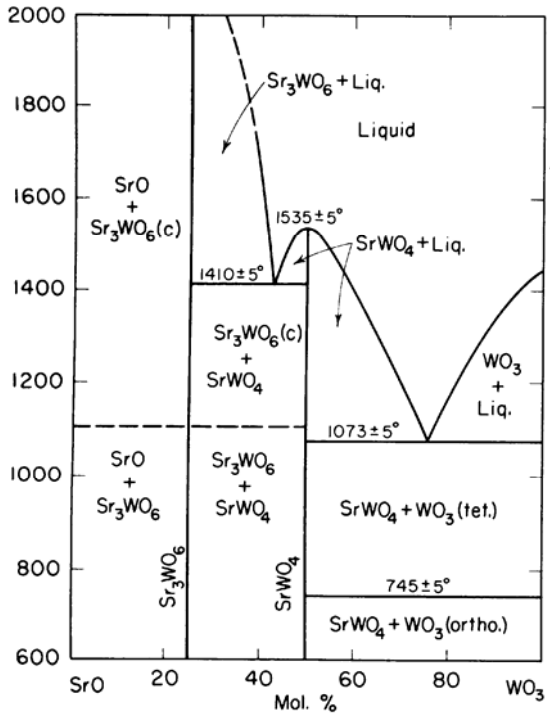

SrO-WO_3 phase diagram. PEDv2.1 Diagram 2337.

L. L. Y. Chang, M. G. Scroger, B. Phillips, "Alkaline-earth tungstates: equilibrium and stability in the M-W-O systems", *J. Am. Ceram. Soc.*, **49** [7] 385-390 (1996).

SrO-Sm_2O_3-MoO_3

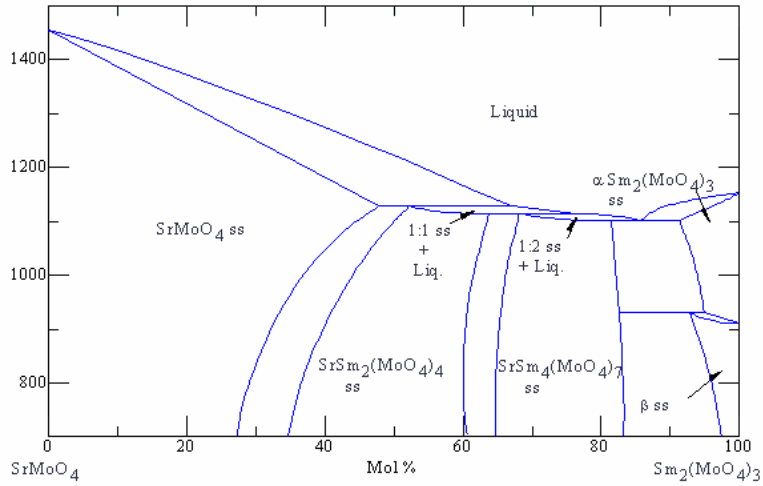

SrO-Sm_2O_3-MoO_3 phase diagram. PEDv2.1 Diagram 6807.

V. V. Vakulyuk, A. A. Evdokimov, T. A. Berezina, "Phase relations in calcium (strontium) molybdate-lanthanide molybdate ($Ca(Sr)MoO_4$-$Ln_2(MoO_4)_3$) systems, where Ln = praseodymium to lutetium", *Zh. Neorg. Khim.*, **27** [7] 1812-1814 (1982).

SrO-TeO_2

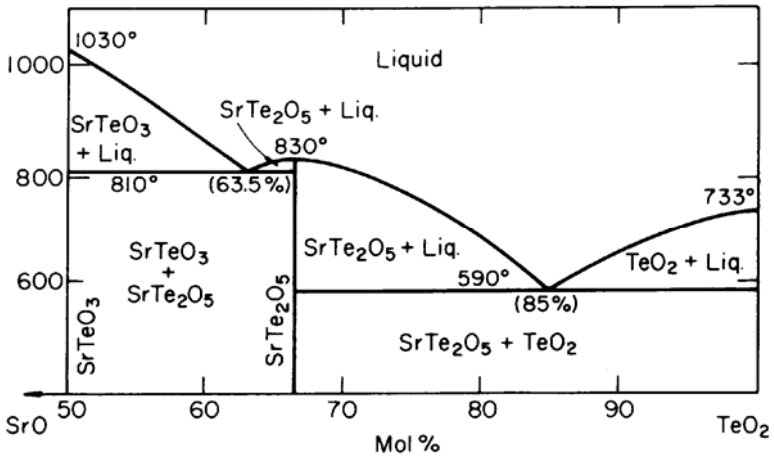

SrO-TeO_2 phase diagram. PEDv2.1 Diagram 5181.

S. A. Malyutin, K. K. Samplavaskaya, M. Kh. Karapet'yants, "Magnesium tellurate-tellurium dioxide and strontium tellurate-tellurium dioxide systems", *Zh. Neorg. Khim.*, **16** [6] 1732-1733 (1971).

$SrO\text{-}Mn_2O_3\text{-}MnO_2$

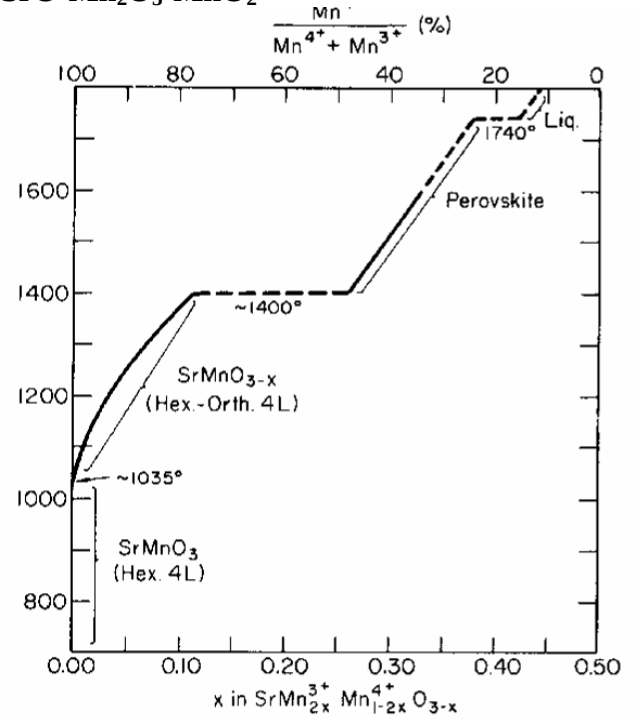

$SrMnO_{3-x}$ phase diagram. PEDv2.1 Diagram 4224.

T. Negas, R.S. Roth, "The System $SrMnO_{3-x}$," *J. Solid State Chem.*, **1** [3-4] 409-418 (1970).

$La_2O_3\text{-}SrO\text{-}Fe_2O_3\text{-}ZrO_2$

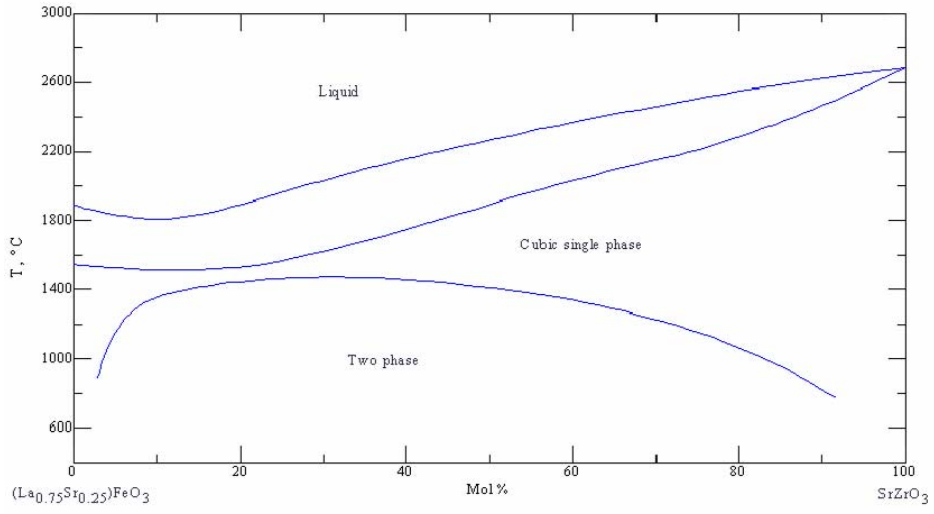

$La_{0.75}Sr_{0.25}FeO_3$- $SrZrO_3$ phase diagram. PEDv2.1 Diagram 91-138.

T. Sasamoto, W.R. Cannon, H. K. Bowen, "Phase Relationships, Electrical Conductivities and Vaporization Rates in the System Lanthanum Chromium Iron Oxide ($La(Fe_{0.5}Cr_{0.5})O_3$)-Strontium Chromium Iron Oxide ($Sr(Fe_{0.5}Cr_{0.5})O_3$)-Strontium Zirconium Zirconate ($SrZrO_3$) in Air," *Ceram. Int.*, **7** [1] 3-7 (1981).

FeO-SrO-Fe_2O_3-La_2O_3

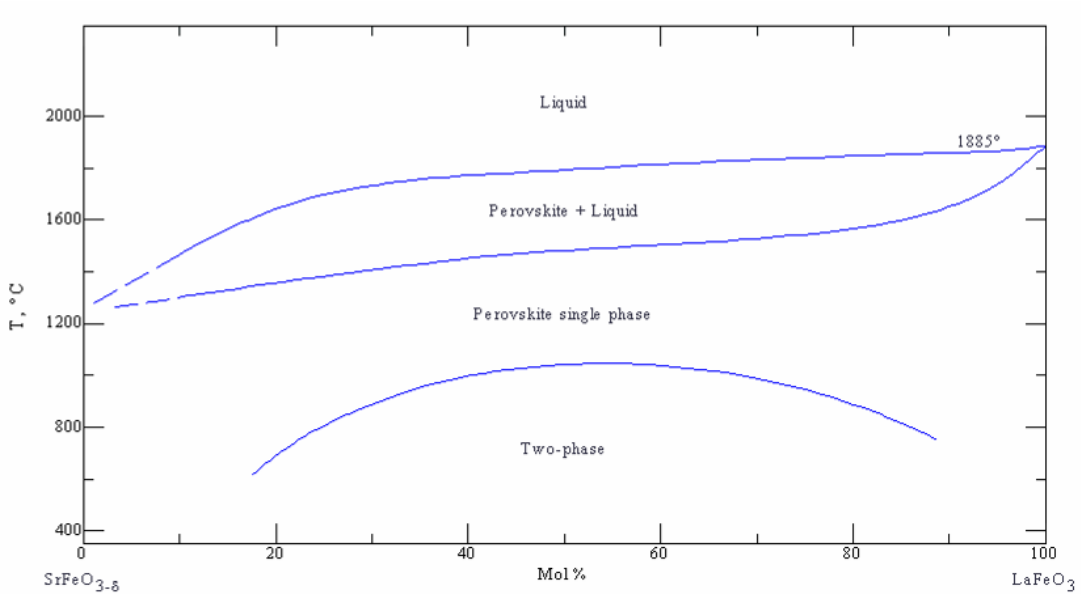

$SrFeO_{3-d}$-$LaFeO_3$ phase diagram. PEDv2.1 Diagram 91-362.

T. Sasamoto, J. Mizusaki, M. Yoshimura, W. R. Cannon, H. K. Bowen, "Phase relationships and electrical conductivity of the perovskite-type solid solutions in the system strontium zirconium trioxide-lanthanum iron trioxide-$SrFeO_{3-d}$ in air," *Yogyo Kyokaishi*, **90** [1] 24-30 (1982).

SrO-TiO_2

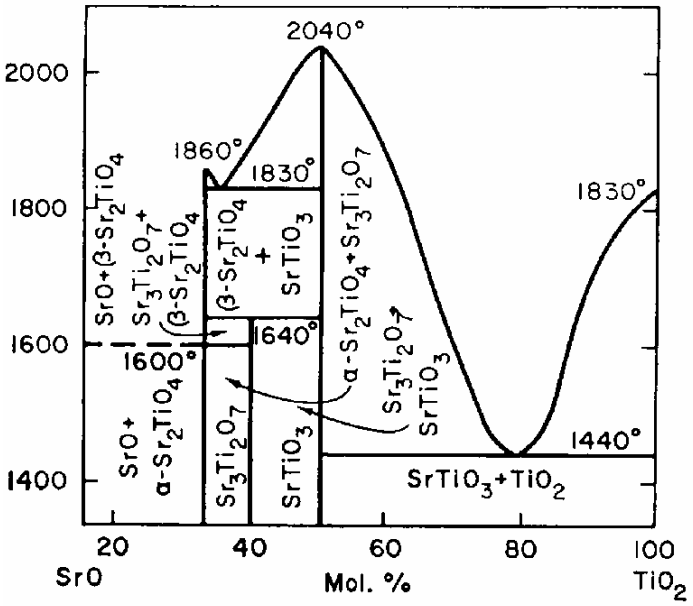

SrO-TiO_2 phase diagram. PEDv2.1 Diagram 0297.

M. Drys, W. Trzebiatowski, "The system strontium oxide-titanium dioxide," *Rocz. Chem.*, **31** [2] 489-496 (1957).

SrO-ZrO_2

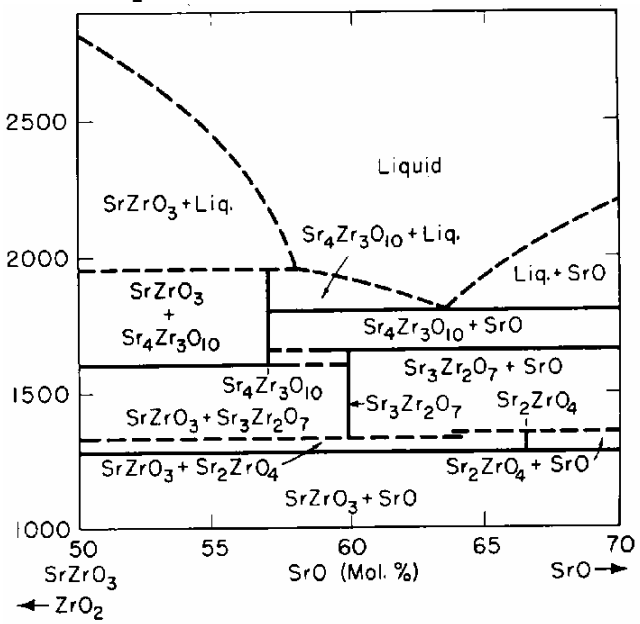

SrO-ZrO_2 phase diagram. PEDv2.1 Diagram 2335.

G. Tilloca, M. Perez y Jorba, "Refractory compounds having structures derived from the perovskite structure in the systems ZrO_2-alkaline earth oxides," *Rev. Hautes Temp. Refract.*, **1** [4] 331-342 (1964).

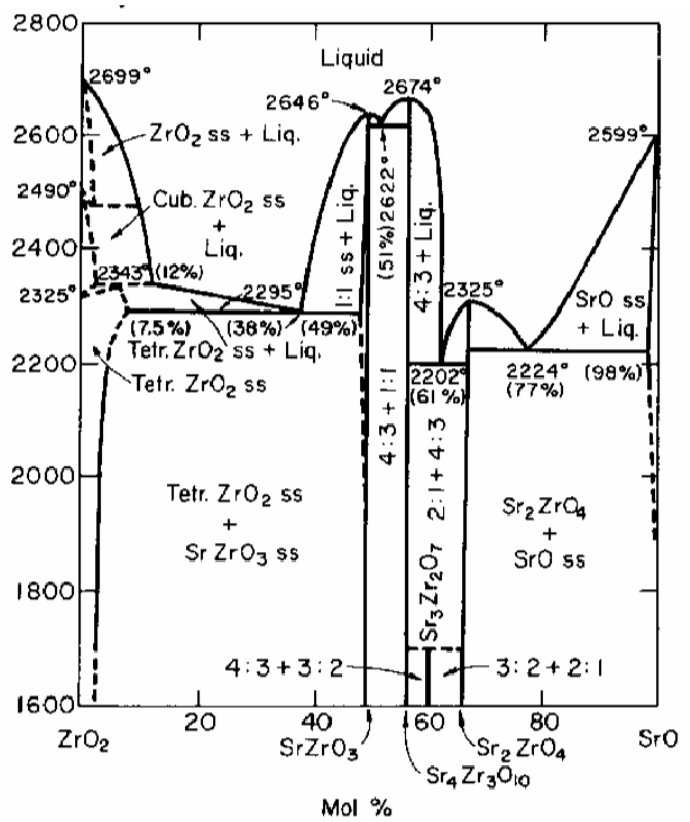

SrO-ZrO_2 phase diagram. PEDv2.1 Diagram 4361.

T. Noguchi, T. Okubo, O. Yonemochi, "Reactions in the system zirconium dioxide-strontium oxide," *J. Am. Ceram. Soc*., **52** [4] 178-181 (1969).

PbO-TiO_2-ZrO_2

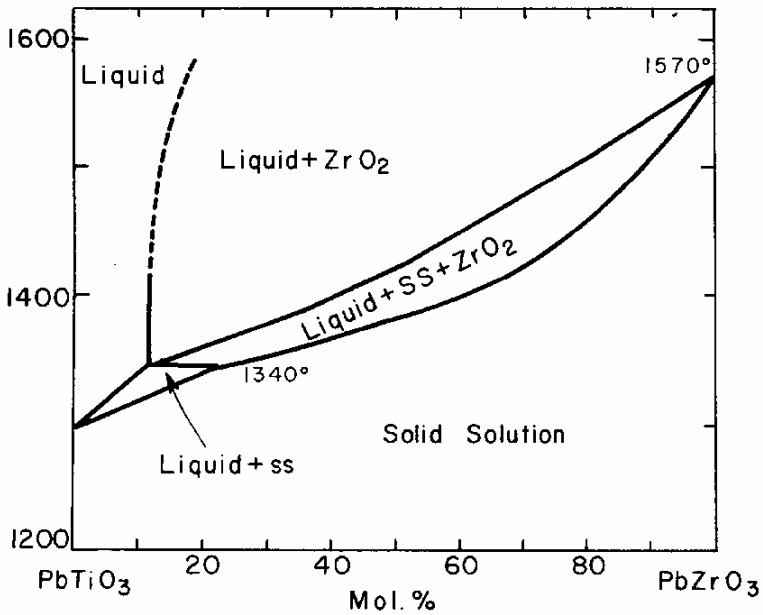

PbO-TiO_2-ZrO_2 phase diagram. PEDv2.1 Diagram 2560.

S. Fushimi, T. Ikeda, "Phase equilibrium in the system PbO-TiO_2-ZrO_2," *J. Am. Ceram. Soc.*, **50** [3] 129-132 (1967).

PbO-TiO_2

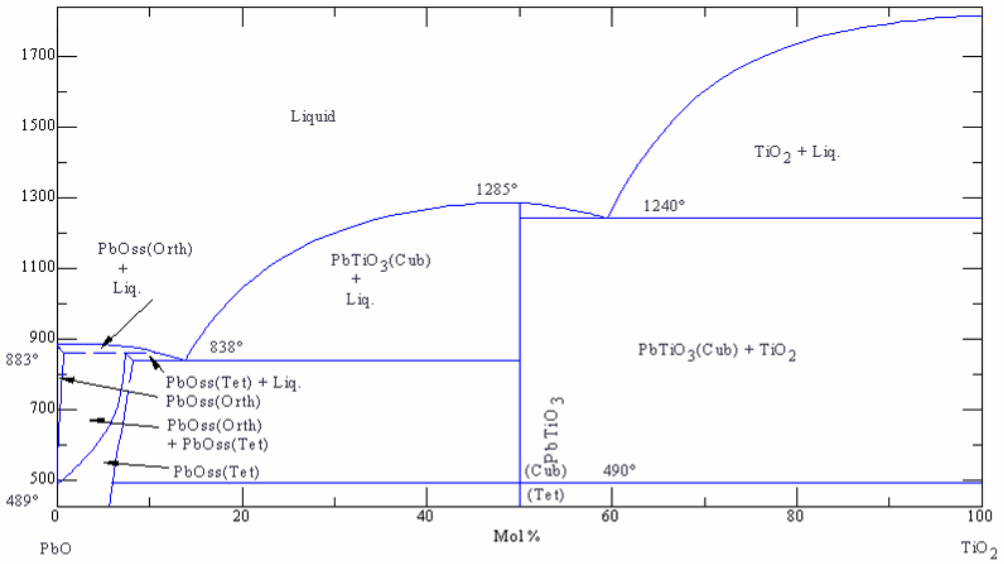

PbO-TiO_2 phase diagram. PEDv2.1 Diagram 6425.

M. A. Eisa, M. F. Abadir, A. M. Gadalla, "The system titanium dioxide-lead-oxygen in air," *Trans. J. Br. Ceram. Soc.*, **79** [4] 100-104 (1980).

BaO-TiO_2

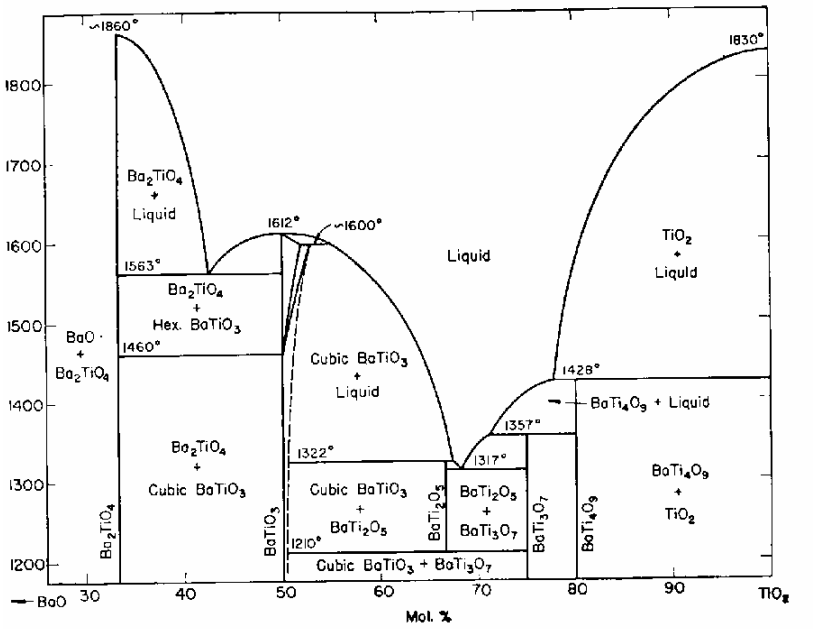

BaO-TiO_2 phase diagram. PEDv2.1 Diagram 0213.

D. E. Rase, R. Roy, Eighth Quarterly Progress Report, April 1- June 30, Appendix II, The Pennsylvania State University, College of Mineral Industries; University Par, pp. 32 (1953).

Cr_2O_3-La_2O_3

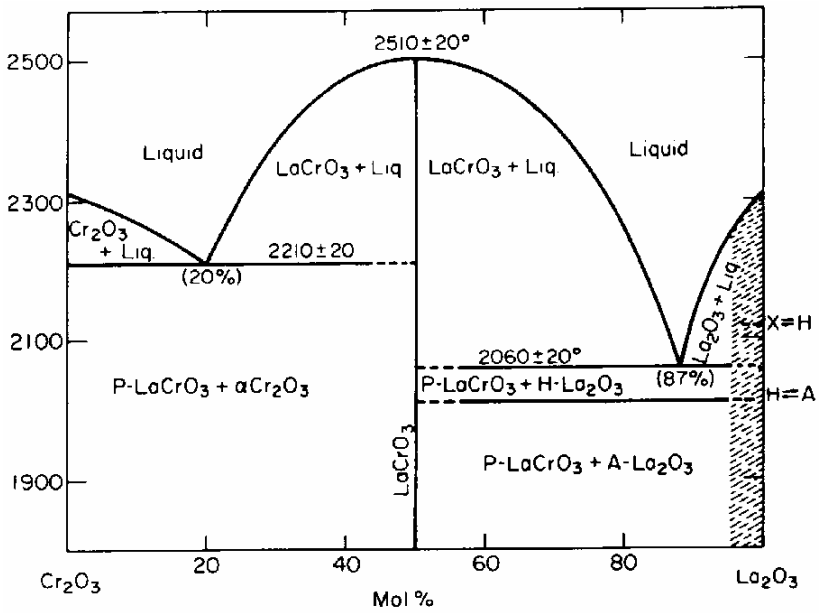

Cr_2O_3-La_2O_3 phase diagram. PEDv2.1 Diagram 5202.

R. Berjoan, "Contribution to the study od interactions between oxygen and lanthanum oxide, chromium (III) oxide or lanthanum chromite," *Rev. Int. Hautes Temp. Refract.*, **13** [2] 119-135 (1976).

Fe_2O_3-CaO-La_2O_3

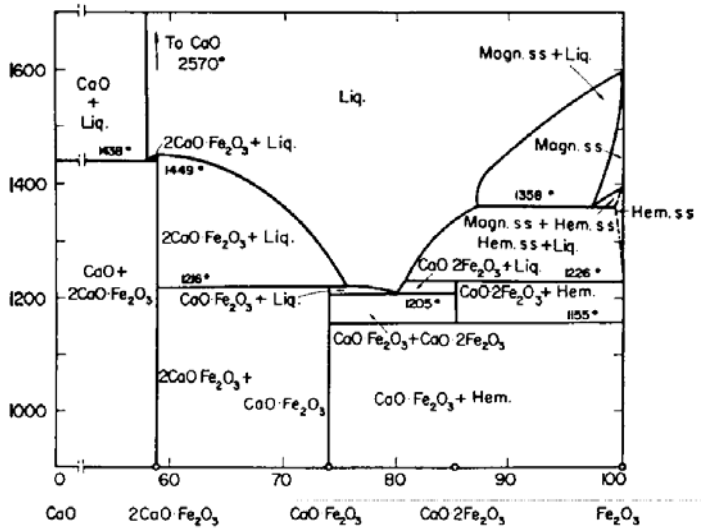

Fe_2O_3-CaO-La_2O_3 phase diagram. PEDv2.1 Diagram 0043.

B. Phillips, A. Muan, "Phase equilibriums in the system calcium oxide-iron oxide in air and at 1 atmosphere oxygen pressure," *J. Am. Ceram. Soc.*, **41** [11] 445-454 (1958).

La_2O_3-CuO-SrO

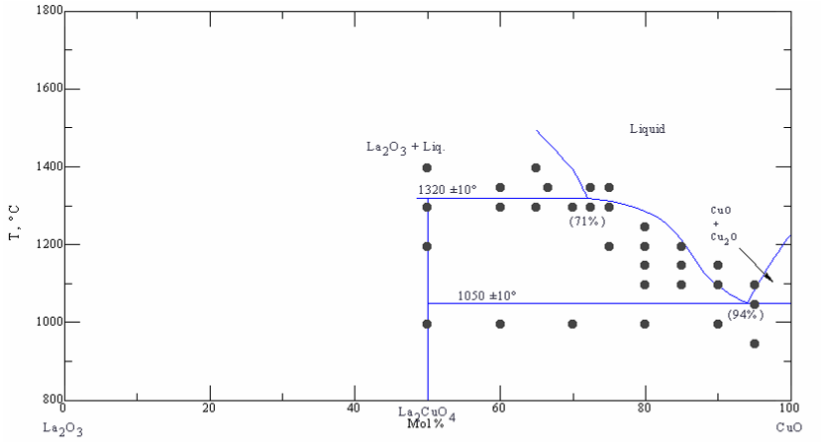

La_2O_3-CuO phase diagram. PEDv2.1 Diagram S-048.

K. Oka, H. Unoki, "Phase diagram of the La2O3-CuO system and crystal growth of (LaBa)2CuO4," *Jpn. J. Appl. Phys. Part 2*, **26** [10] L1590-1592 (1987).

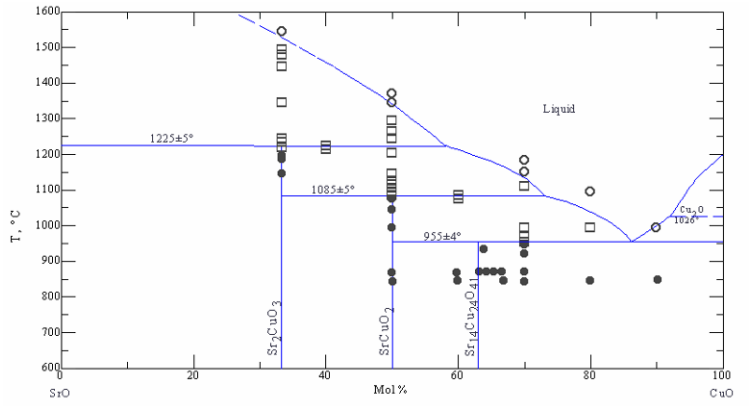

SrO-CuO phase diagram. PEDv2.1 Diagram S-053.

N. M. Hwang, R. S. Roth, C. J. Rawn, "Phase Equilibria in the systems SrO-CuO and SrO-1/2Bi_2O_3," *J. Am. Ceram. Soc.*, **73** [8] 2531-2533 (1990).

V_2O_5-CuO

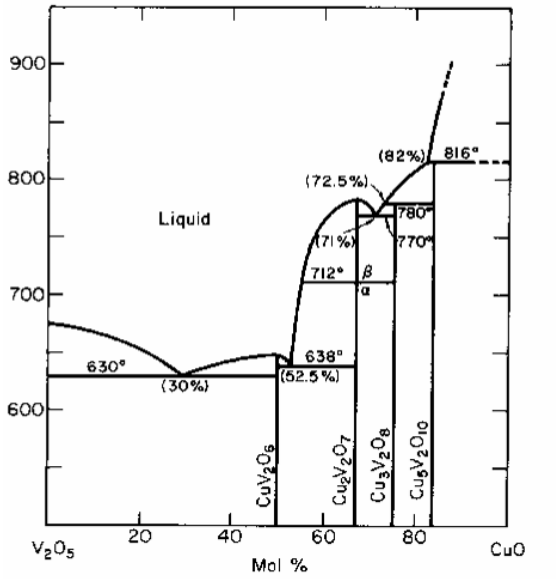

V_2O_5-CuO phase diagram. PEDv2.1 Diagram 4326.

P. Fleury, "CuO-V_2O_5 system," *C. R. Seances Acad. Sci., Ser. C*, **263** [22] 1375-1377 (1966).

CaO-CuO

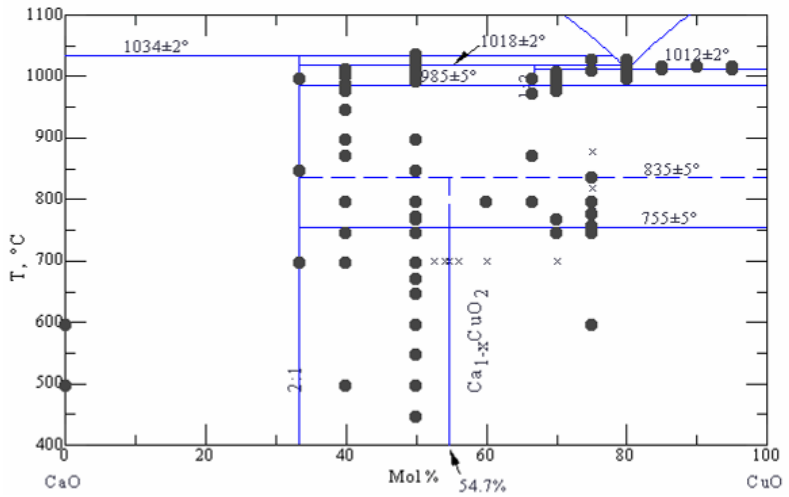

CaO-CuO phase diagram. PEDv2.1 Diagram S-187A of A-B.

R. S. Roth, C. J. Rawn, J. J. Ritter, B. P. Burton, "Phase equilibria of the system SrO-CaO-CuO," *J. Am. Ceram. Soc.*, **72** [8] 1545-1549 (1989).

CuO-Bi_2O_3

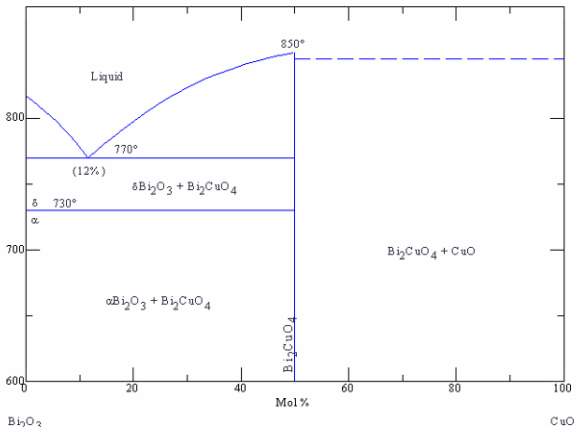

CuO-Bi_2O_3 phase diagram. PEDv2.1 Diagram 6392.

B. G. Kakhan, V. B. Lazarev, I. S. Shaplygin, "Study of the subsolidus part of phase diagrams of Bi_2O_3-MO binary systems (M = nickel, copper, or palladium)," *Zh. Neorg. Khim.*, **24** [6] 1663-1668 (1979).

CuO-CoO

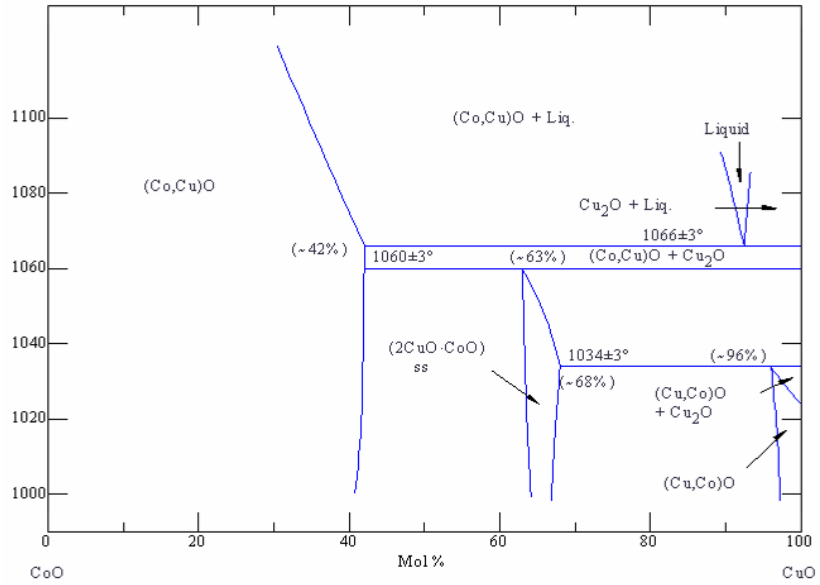

CuO-CoO phase diagram. PEDv2.1 Diagram 6540A of A-B.

C. Landolt, A. Muan, "Activity-composition relations in copper oxide-cobalt oxide solid solutions as determined from equilibria in the copper-cobalt-oxygen system," *J. Inorg. Nucl. Chem.*, **31** [5] 1319-1326 (1969).

CuO-MoO_3

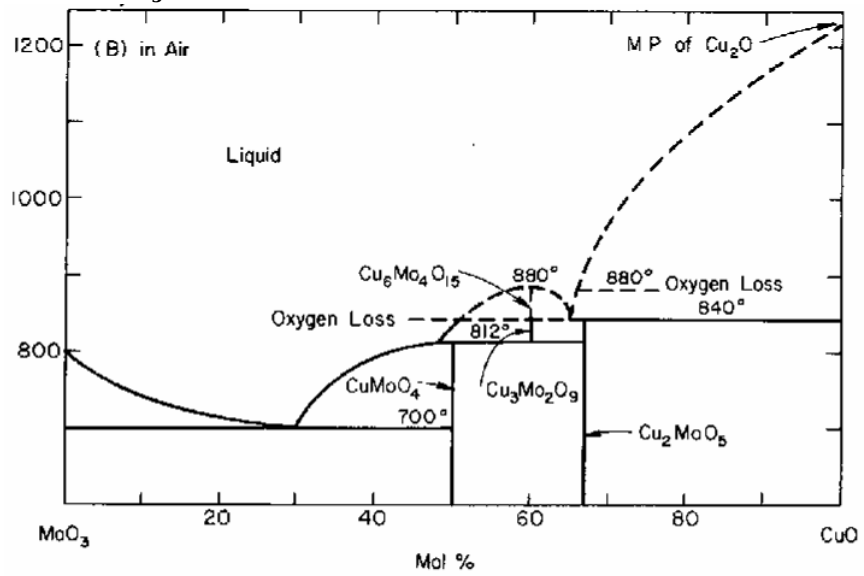

CuO-MoO_3 phase diagram. PEDv2.1 Diagram 4196.

K. Nassau, J. W. Shiever, "Cupric oxide-molybdenum oxide phase diagram in air and in oxygen," *J. Am. Ceram. Soc.*, **52** [1] 36-40 (1969).

CuO-Al_2O_3

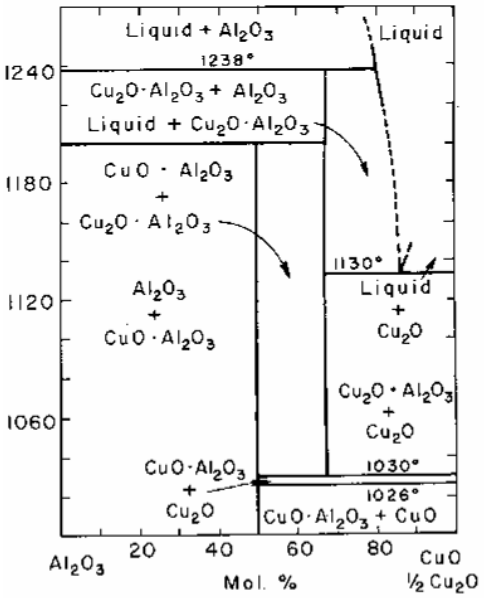

$CuO-Al_2O_3$ phase diagram. PEDv2.1 Diagram 2087.

A. M. M. Gadalla, J. White, "Equilibrium relations in the system Cu2O-CuO-Al2O3," *Trans. Br. Ceram. Soc*., **63** [1] 39-62 (1964).

CuO-TeO_2

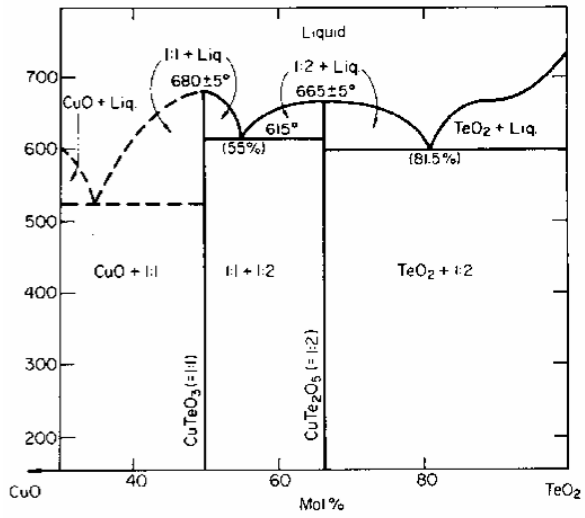

$CuO-TeO_2$ phase diagram. PEDv2.1 Diagram 5151.

I. Ivanova, M. Marinov, Y. B. Dimitriev, "Phase diagram and electrical properties in the copper(II) oxide-tellurium(IV) oxide system," *Dokl. Bolg. Akad. Nauk*, **25** [10] 1391-1394 (1972).

CuO-GeO_2

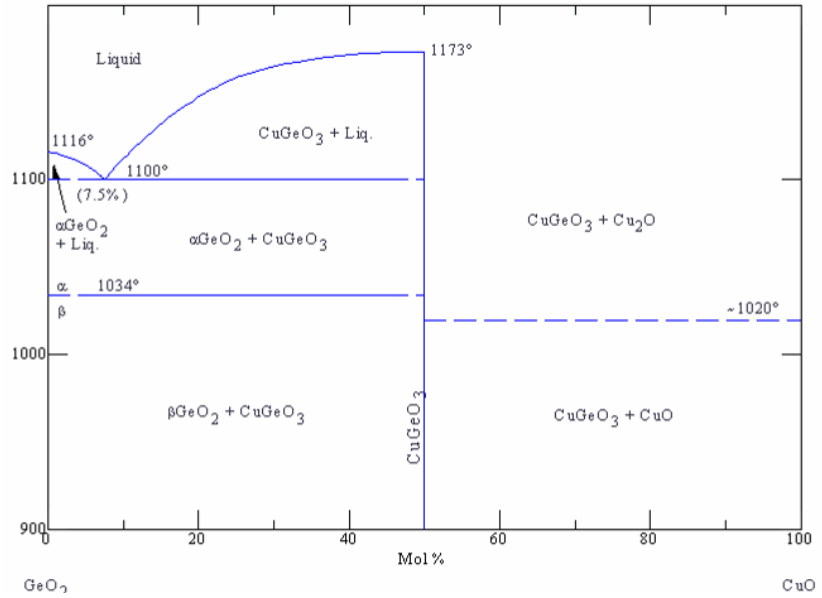

CuO-GeO_2 phase diagram. PEDv2.1 Diagram 6393.

E. I. Speranskaya, "The CuO-GeO2 and Cu2O-GeO2 systems," *Izv. Akad. Nauk SSSR, Neorg. Mater.*, **3** [8] 1458-1466 (1967).

CuO-B_2O_3

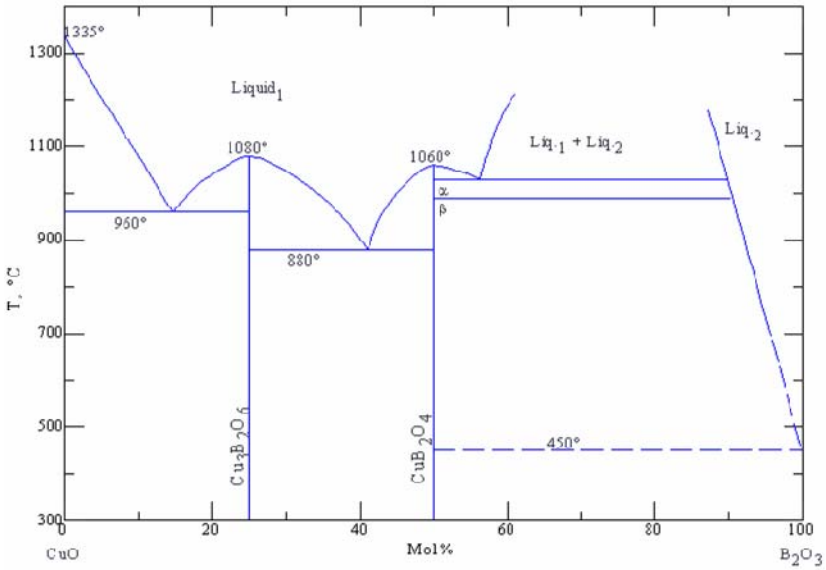

CuO-B_2O_3 phase diagram. PEDv2.1 Diagram 93-006

G. K. Abdullaev, P. F. Rza-Zade, Kh. S. Mamdov, "Physiochemical study of a lithium oxide-copper(II) oxide-boron oxide ternary system," *Zh. Neorg. Khim.*, **27** [7] 1837-1841 (1982).

CuO-BaO

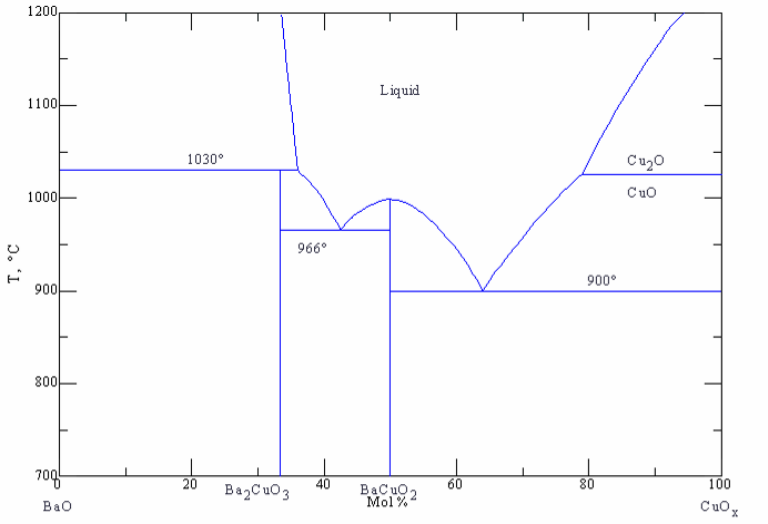

CuO-BaO phase diagram. PEDv2.1 Diagram S-011.

B. J. Lee, D. N. Lee, "Calculation of phase diagrams for the $YO_{1.5}$-BaO-CuO_x system," J. Am. Ceram. Soc., **72** [2] 314-319 (1989).

BaO-Fe_2O_3

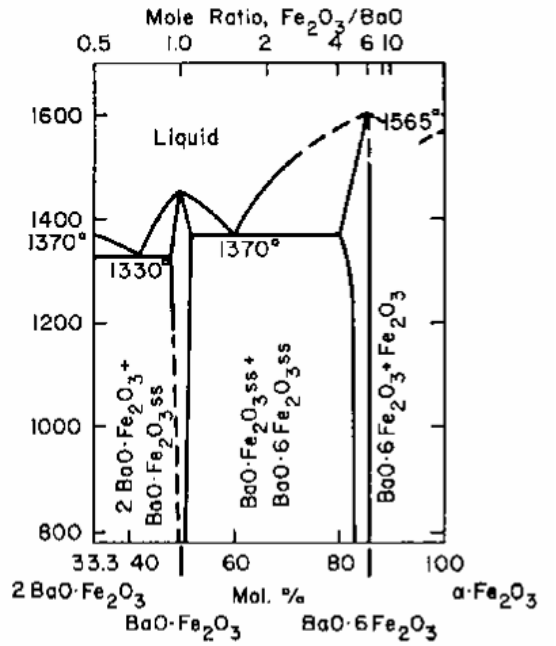

BaO-Fe_2O_3 phase diagram. PEDv2.1 Diagram 0208.

Y. Goto, T. Takada, "Phase diagram of the system BaO-Fe_2O_3," *J. Am. Ceram. Soc.*, **43** [3] 150-153 (1960).

MnO-SiO_2-CaO

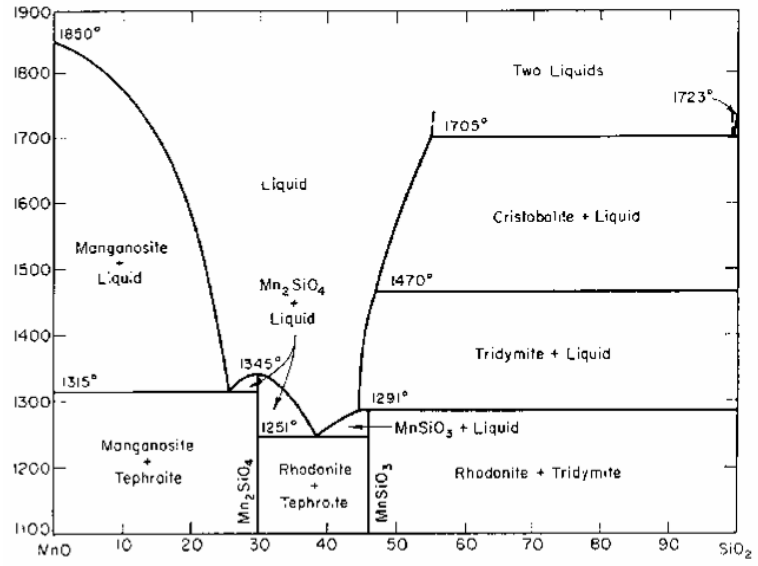

$MnO-SiO_2$ phase diagram. PEDv2.1 Diagram 0101

J. White, D. D. Howatt, and R. Hay, "The binary system $MnO-SiO_2$," *J. R. Tech. Coll. (Glasgow)*, **3**, 231-240 (1934).

MnO-V_2O_5

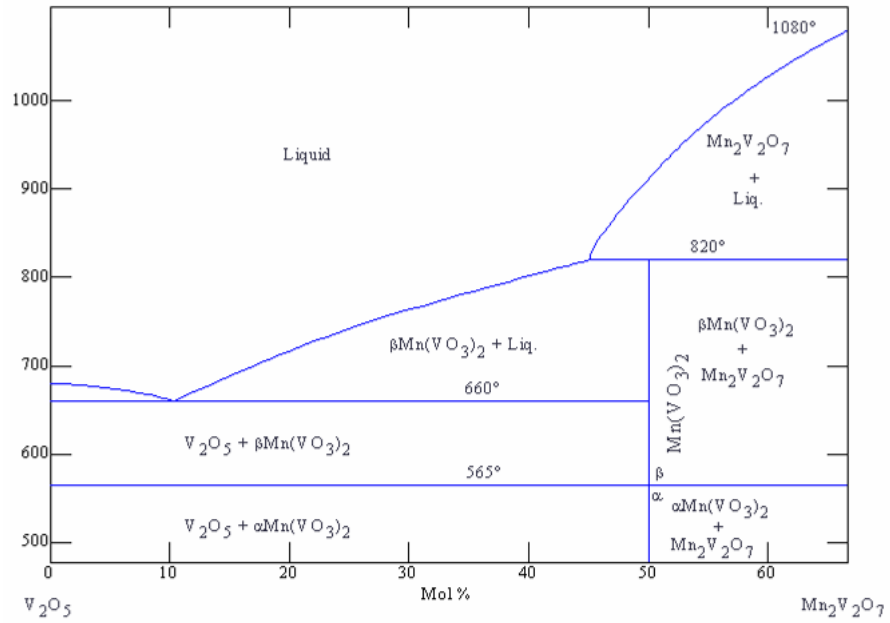

$MnO-V_2O_5$ phase diagram. PEDv2.1 Diagram 6412.

A. A. Fotiev, L. L. Surat, "Phase diagram of the vanadium oxide (V_2O_5)-manganese vanadate ($Mn_2V_2O_7$) system," *Zh. Neorg. Khim.*, **27** [4] 1078-1079 (1982).

MnO-Al_2O_3

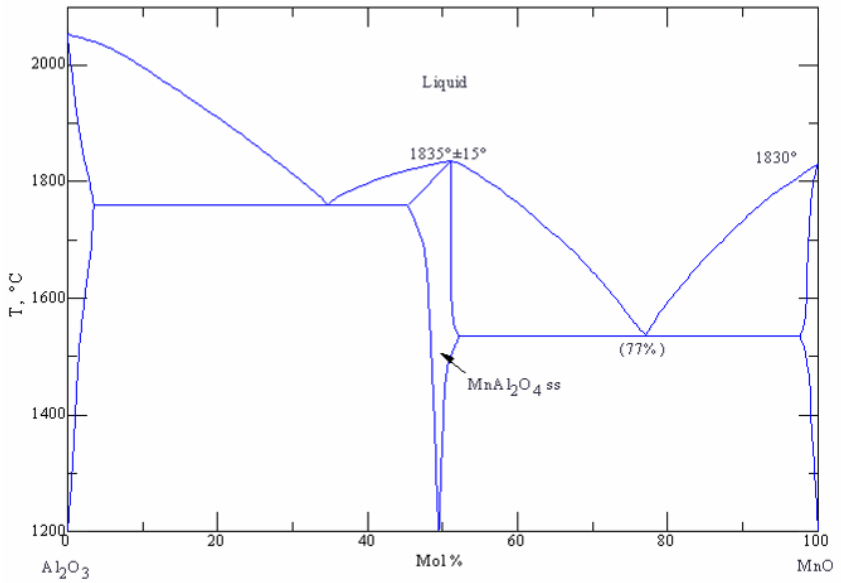

$MnO-Al_2O_3$ phase diagram. PEDv2.1 Diagram 92-004.

K. T. Jacob, "Revision of thermodynamic data on manganese(II) oxide-aluminum oxide," *Can. Metall. Q.*, **20** [1] 89-92 (1981).

CaO-MnO-GeO_2

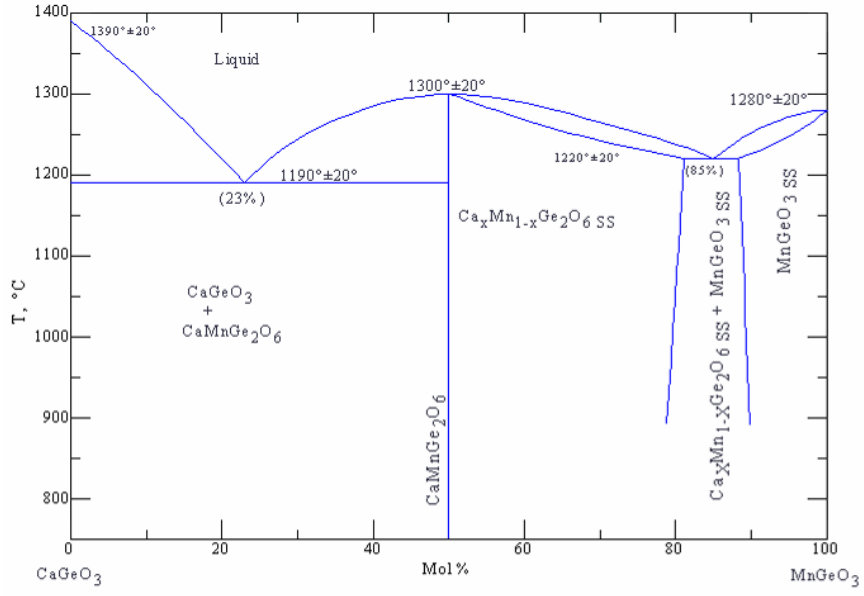

$CaO-MnO-GeO_2$ phase diagram. PEDv2.1 Diagram 93-113.

G. A. Mikirticheva, L. F. Grigor'eva, R. G. Grebenshchikov, "Phase equilibriums in a calcium germanate-manganese germanate ($CaGeO_3$-$MnGeO_3$) system," *Izv. Akad. Nauk. SSSR, Neorg. Mater.*, **16** [11] 2009-2013 (1980).

Fe_2O_3-V_2O_5

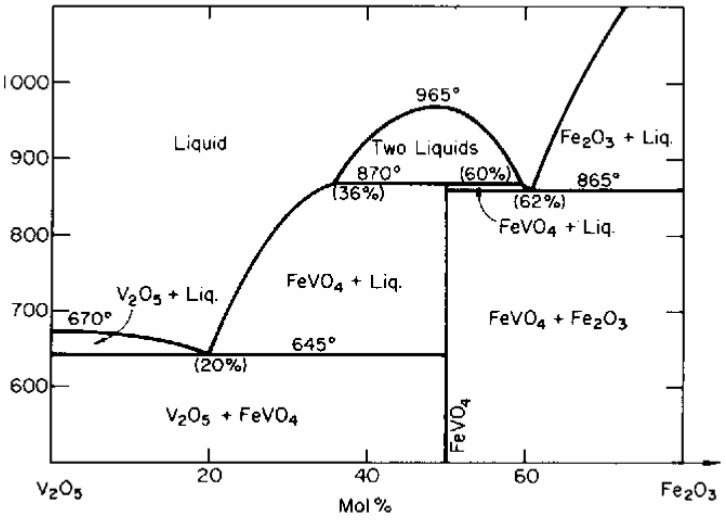

Fe_2O_3-V_2O_5 phase diagram. PEDv2.1 Diagram 5220.

R. C. Kerby, J. R. Wilson, "Solid-liquid phase equilibriums for the ternary systems vanadium(V) oxide-sodium oxide-iron(III) oxide, vanadium(V) oxide-sodium oxide-chromium (III) oxide, and vanadium(V) oxide-sodium oxide-magnesium oxide," *Can. J. Chem.*, **51** [7] 1032-1040 (1973).

Fe_2O_3-Ga_2O_3

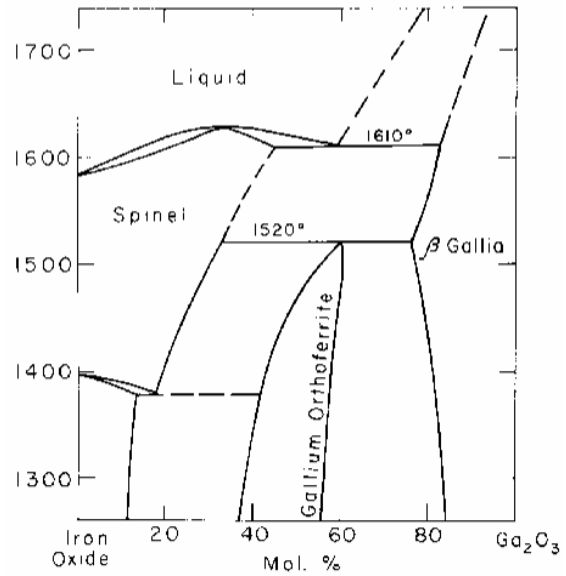

Fe_2O_3-Ga_2O_3 phase diagram. PEDv2.1 Diagram 2149.

H. J. Van Hook, "Thermal stability of gallium orthoferrite in the system Fe_2O_3-FeO-Ga_2O_3," *J. Am. Ceram. Soc.*, **48** [9] 470-472 (1965).

CoO-Bi_2O_3-Fe_2O_3

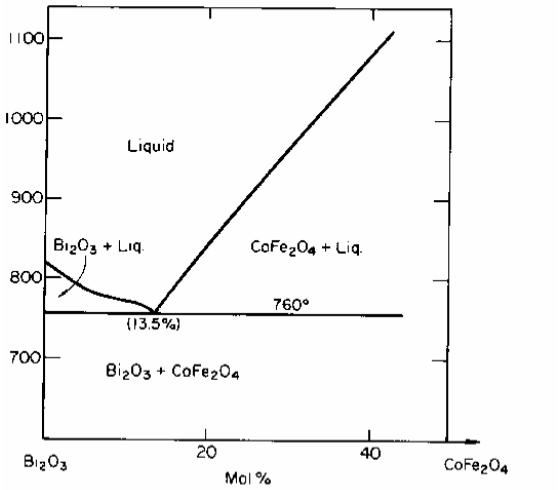

CoO-Bi_2O_3-Fe_2O_3 phase diagram. PEDv2.1 Diagram 5402.

L. M. Viting, G. P. Golubkova, "Reactions of ferrites with bismuth trioxide melt," *Vestn. Mosk. Univ., Ser. 2: Khim.*, **20** [6] 69-70 (1965).

MgO-TiO_2

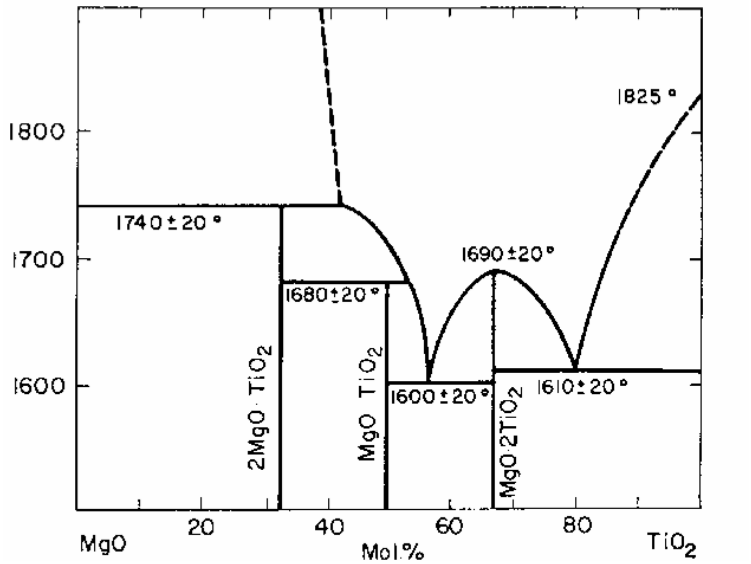

MgO-TiO_2 phase diagram. PEDv2.1 Diagram 0269.

F. Massazza, E. Sirchia, "The system MgO-SiO2-TiO2. I. Revision of the binary systems," *Chim. Ind. (Milan)*, **40** [5] 376-380 (1958).

CaO-TiO_2

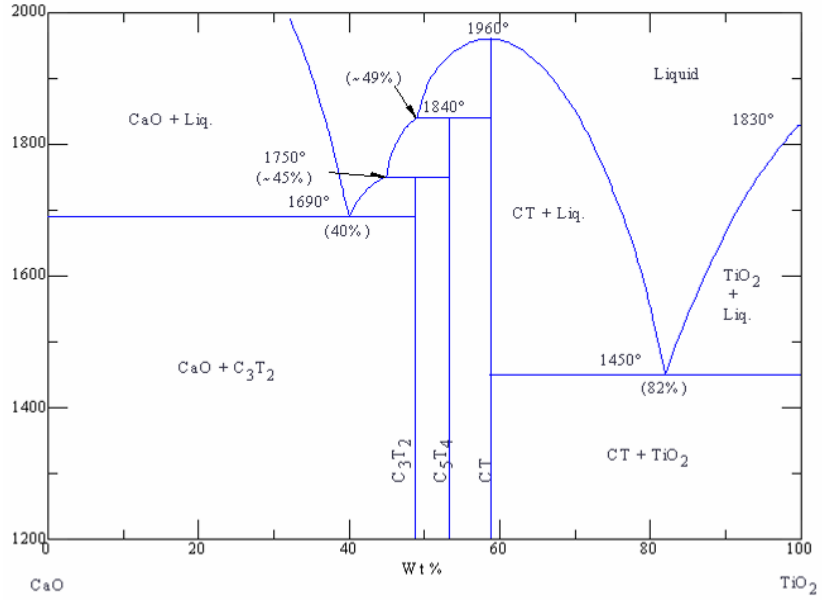

$CaO-TiO_2$ phase diagram. PEDv2.1 Diagram 6385.

H. E. Tulgar, "Solid state relationships in the system calcium oxide-titanium dioxide," *Istanbul Tek. Univ. Bul.*, **29** [1] 111-129 (1976).

MnO-TiO_2

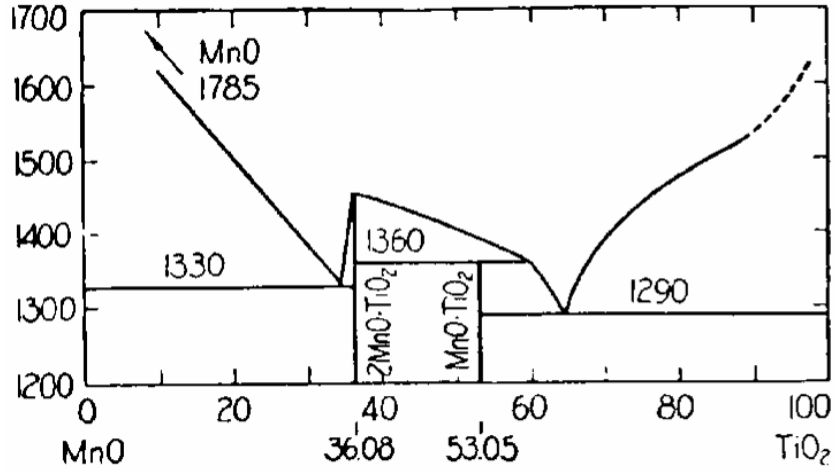

$MnO-TiO_2$ phase diagram. PEDv2.1 Diagram 0277.

J. Grieve, J. White, "The systems MnO-TiO2 and MnO-FeO-TiO2," *J. R. Tech. Coll. (Glasgow)*, **4**, 660-670 (1940).

CoO-TiO_2

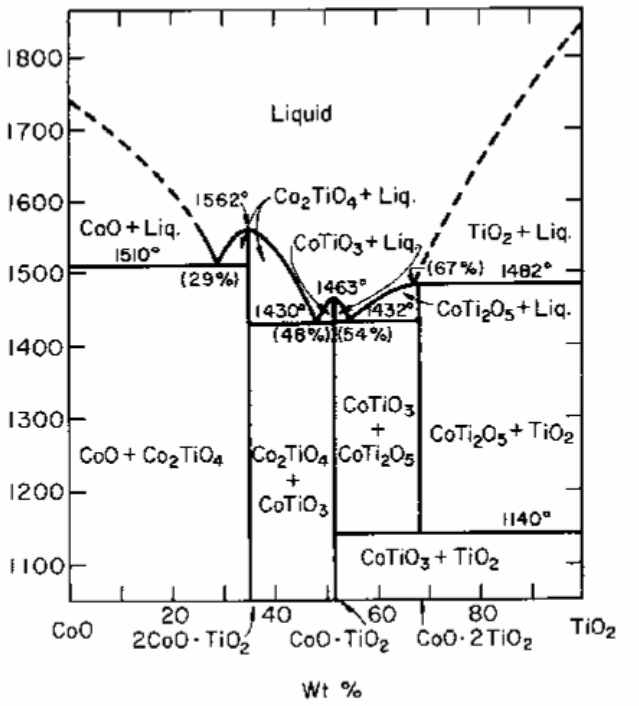

CoO-TiO_2 phase diagram. PEDv2.1 Diagram 4324.

B. Brezny, A. Muan, "Phase relations and stabilities of comounds in the system cobaltous oxide-titanium dioxide," *J. Inorg. Nucl. Chem.*, **31** [3] 649-655 (1969).

Ga_2O_3-TiO_2

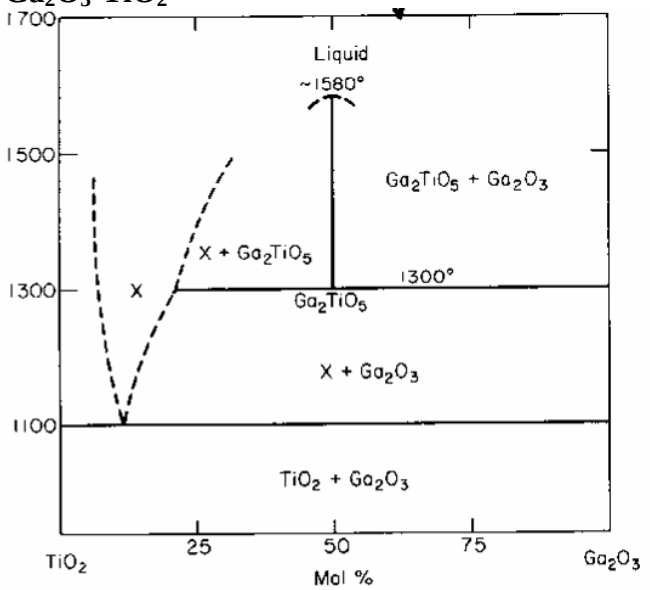

Ga_2O_3-TiO_2 phase diagram. PEDv2.1 Diagram 4412.

A. M. Lejus, D. Goldberg, A. Revcolevschi, "New compounds formed between rutile, TiO2, and oxides of trivalent and quadrivalet metals," *C. R. Seances Acad. Sci., Ser. C*, **263** [20] 1223-1226 (1966).

Examples of common materials where some of these systems can be applied are:

$PbTiO_3$
$BaTiO_3$
$La_xCa_{1-x}FeO_3$
$La_xSr_{1-x}MnO_3$
$La_xSr_{1-x}FeO_3$
$La_xSr_{1-x}Co_yFe_{1-y}O_3$
$La_xSr_{1-x}Ga_yMg_{1-y}O_3$
$La_xCa_{1-x}MnO_3$
$La_xSr_{1-x}CrO_3$
$LaCrO_3$
$SrTiO_3$
$SrZrO_3$
$PbZr_xTi_{1-x}O_3$
$LaMnO_3$